TRC

ELARD

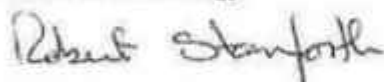# ESIA Review

Independent 3rd Party Assessment of the Impacts on Water Resources and Geology, Biodiversity and Air Quality

July 22, 2019

Amulsar Gold Mine
The Republic of Armenia

Prepared For:

Investigative Committee of the Republic of Armenia

Prepared By:

ELARD
Beirut, Lebanon

TRC
New Providence, New Jersey, USA

Prepared by: David Hay, PhD, CPG
Water Resources and Geology

Prepared by: Robert Stanforth, PhD
Water Resources and Geology

Prepared by: Carla Khater, PhD
Biodiversity

Prepared by: Alexandra Cluchier, MSc, EPHE
Biodiversity

Prepared by: Charbel Afif, PhD
Air Quality

Reviewed & Approved by: Nidal Rabah, PhD, PE, PM
Water Resources and Geology

Reviewed & Approved by: Ramez Kayal, MSc
Water Resources and Geology

Reviewed & Approved by: Ricardo Khoury, ME
Biodiversity and Air Quality

TABLE OF CONTENTS

TABLES

FIGURES

APPENDICES

Appendix A: Amulsar Block Physiographic Map and Geologic Map of Vayots and Faults Alignments
Appendix B: Map Showing Hydraulic Conductivity Test Locations
Appendix C: Lydian's Responses (April 2019) to ELARD Team Inquiry (Geochemical Model Input Data & Phases and Lydian Press Release about Amulsar Mine Groundbreaking)

ACRONYM LIST

Acidity

ABA	Acid-Base Accounting
AMD	Acid Mine Drainage
AP	Potential Acidity
ARD	Acid Rock Drainage
NAG	Net Acid Generation
NPR	Net Potential Ratio
NP	Acid Neutralizing Capacity
Non-PAG	Non-Potentially Acid Generating
NNP	Net Neutralization Potential
PAG	Potentially Acid Generating
SAG	Strongly Acid Generating
WAD	Weak Acid Dissociable

Chemistry

DO	Dissolved Oxygen
C	Carbon
$CaCO_3$	Carbonate
CaO	Lime
CO_2	Carbon dioxide
H	Hydrogen
HCl	Hydrochloric acid
K	Potassium
N	Nitrogen
NaCN	Sodium cyanide
NaOH	Sodium hydroxide
NH_4	Ammonia
NO_3	Nitrate
O	Oxygen
Fe	Iron
Fe(III)	Ferric Iron (Fe^{3+})
Fe(II)	Ferrous Iron (Fe^{2+})
S	Sulfur
Si	Silicon
Sr	Strontium

Geology & Hydrogeology

ET	Evapotranspiration
K_h	Horizontal Hydraulic Conductivity
K_v	Vertical Hydraulic Conductivity

K_h / K_v	Hydraulic Conductivity Anisotropy Ratio
LV	Lower Volcanics
LVA	Lower Volcanic Andesite
VC	Upper Volcanics (a.k.a. UV)

Laboratory/Chemical Analyses & Testing

AAS	Atomic Absorption Spectroscopy
COC	Constituent of Concern
HC	Humidity Cell
ICP	Inductively-coupled Plasma
SPLP	Synthetic Precipitation Leaching Procedure
XRD	X-Ray Diffraction
XRF	X-Ray Fluorescence
Wt.	Weight
Wt.%	Percentage by weight

Mining

ADR	Adsorption/Desorption/Recovery
BLS	Barren Leach Solution
BRSF	Barren Rock Storage Facility
GARD Guide	Global Acid Rock Drainage Guide
HL	Heap Leach
HLF	Heap Leach Facility
HLP	Heap Leach Pad
HLS	Heap Leach Solution
PLS	Pregnant Leach Solution
PSP	Pregnant Solution Pond

Miscellaneous

ASCE	American Society of Civil Engineers
ASL	Above Sea Level
ASTM	American Society for Testing and Materials
ATB	Amulsar Tectonic Block
EBRD	European Bank for Reconstruction and Development
ELARD	Earth Link & Advanced Resources Development
EMP	Environmental Monitoring Plan
RA	Republic of Armenia
ESIA	Environmental & Social Impact Assessment
EIA	Environmental Impact Assessment
GRE	Global Resource Engineering Ltd.
GSA	Groundwater Study Area
IBC	International Building Code

INAP	International Network for Acid Prevention
ICRA	Investigative Committee of the Republic of Armenia
IFC	International Finance Corporation
IPCC	Intergovernmental Panel on Climate Change
ITRC	Interstate Technical & Regulatory Counsel (USA)
MNP	RA Ministry of Nature Protection
LCRS	Leak Collection and Recovery System
OM&M	Operation, Maintenance & Monitoring
PTS	Passive Treatment System
Q	Quarter
RA	The Republic of Armenia
SNCO	Environmental Monitoring and Information Center" of the RA MNP
SWWB	Site-Wide Water Balance
TOR	Terms of Reference (dated November 27, 2018 for this project)
TRC	TRC Environmental Corporation
UNDP	United Nations Development Programme
USEPA	United States Environmental Protection Agency
1D	One-dimensional
2D	Two-dimensional
3D	Three-dimensional

Biodiversity

ASCI	Areas of Special Conservation Interest
BOS	Biodiversity Offset Strategy
HIU	Habitats Impact Unit
IBA	Important Bird Area
IPA	Important Plant Area
JNP	Jermuk National Park
KBA	Key Biodiversity Area
NNL	No Net Loss

Air Quality

CO	Carbon Monoxide
DMRB	Design Manual for Roads and Bridges
HCl	Hydrochloric Acid
HCN	Hydrogen Cyanide
Hg	Mercury
MPC	Maximum Permissible Concentration
NOx	Nitrogen Oxides
PM	Particulate Matter
SO_2	Sulfur Dioxide
SOP	Standard Operating Procedure

| TSP | Total Suspended Particles |
| WHO | World Health Organization |

Units

km	kilometer
m	meter
mg/L	Milligram per liter
mm	millimeter
mM	milliMolar
mm/year	millimeter per year (mm/yr)
m^3	cubic meter
m^3/year	cubic meter per year

1.0 Introduction

Earth Link & Advanced Resources Development (ELARD) in association with TRC Environmental Corporation (ELARD-TRC Team) was retained by the Investigative Committee of the Republic of Armenia (ICRA), to conduct an independent, third-party assessment of the impacts of the Amulsar Mine on water resources and geology, biodiversity and air quality. The Amulsar Mine ("Site", "Mine", or "Project") is located in central south-east Armenia and is being developed by Lydian International (Lydian).

This Report presents the results of ELARD-TRC Team's assessment of Amulsar Mine's impacts on water resources, geology, biodiversity and air quality pursuant to the November 27, 2018 Terms of Reference (TOR).

1.1 Objectives

Pursuant to the TOR, the objectives of the Independent Assessment are to:

On Water Resources and Geology:

- Evaluate the extent, methodologies, and scientific rigor of data collection, and the reliability of the conclusions of the Environmental and Social Impact Assessment (ESIA; version 10; June 2016) and Environmental Impact Assessment (EIA) related to water and geology;

- Evaluate the appropriateness of ESIA/EIA assessment of risks on water resources and geology and the appropriateness of proposed monitoring and mitigation measures including effectiveness and compliance with local regulations and international standards;

- Assess data gaps and their impacts on the methodologies of the ESIA/EIA; and

- Provide responses to specific questions included in the TOR.

On Biodiversity:

- Understand and evaluate the impacts of the project on natural habitats and biodiversity;

- Conduct a due diligence study of the existing EIA to ascertain compliance with international standards on preservation and conservation of biodiversity;

- Evaluate the conservation status of patrimonial species (endemic, vulnerable, rare) including *Potentilla Acantholimon* and *Parnassius* among others; and

- Assess the measures proposed for reduction/avoidance of ecological impacts from the project.

- Provide responses to specific questions included in the TOR.

On Air Quality:

- Review the adequateness of the data used to assess the air quality impacts;

- Evaluate the appropriateness of the ESIA/EIA assessment of the impacts from dust generation and its possible health effects taking into account where relevant the chemical composition of dust and the health impact on the surrounding community;

- Evaluate the appropriateness of the air dispersion modeling studies;

- Evaluate the adequacy of the mitigation measures proposed;

- Provide responses to specific questions included in the TOR.

1.2   Scope of Assessment

Pursuant to the TOR, this assessment is mainly based on relevant ESIA and EIA sections and environmental monitoring reports generated since 2016. The Team also reviewed relevant reports prepared by others and data obtained from the Ministry of Nature Protection (MNP) and from internet search and from other experts.

ELARD-TRC Team conducted the following activities:

- Visited the Republic of Armenia during March 26 through 30, 2019 and met with and gave presentations about the scope, goals, and expectations of the Independent Assessment to representatives of ICRA, MNP, and experts from various RA institutions.

- Attended a presentation on Water Resources on March 28, 2019 by Lydian and its consultants including Global Resource Engineering (GRE) and Golder Associates (Golder) about the Amulsar Mine.

- Conducted a Site visit along with representatives of ICRA, MNP, Lydian, GRE, and Golder on March 29, 2019 and observed some of the existing partial structures and facilities.

- Visited Lydian's laboratory on March 29, 2019, where the Team observed rock cores and attended a presentation by Lydian about the bench scale bio-treatability testing.

- Attended through Skype a presentation on Air Quality by Lydian and its consultants on April 5, 2019.

- Attended through Skype a presentation on Biodiversity by Lydian and its consultants on April 9, 2019.

- Provided questions to Lydian and received Lydian's responses via ICRA in April 2019.

- Submitted to ICRA a Partial Draft Independent Assessment Report dated May 31, 2019.

- Submitted to ICRA a Draft Independent Assessment Report dated June 14, 2019.

- Presented the findings of the Independent Assessment to HE the Prime Minister, ICRA and MNP representatives in Yerevan on June 20 and 21, 2019.

- Participated in a conference call related to water and geology with ICRA, MPN, and Lydian's representatives on June 27, 2019 regarding Lydian's comments about the June 14, 2019 Draft Assessment Report.

- Participated in a conference call related to biodiversity and air quality with ICRA, MPN, and Lydian's representatives on July 1st, 2019 regarding Lydian's comments about the June 14, 2019 Draft Assessment Report.

- Reviewed comments received via ICRA from Lydian on June 28, 2019 (on water and geology) and July 4th (on biodiversity and air quality) about the June 14, 2019 Draft Independent Assessment Report.

- Reviewed Lydian's responses received via ICRA on July 3, 2019 to questions provided on June 28, 2019 by ELARD-TRC Team about geochemical data and mitigation measures.

- Submitted a Final Independent Assessment Report dated July 22, 2019.

1.2.1 Assessment of the Impacts of Geology

Pursuant to the TOR, the objectives of the review are to:

- Understand and evaluate the scientific basis of Lydian's claim that the Amulsar block is an isolated geologic block;
- Evaluate the geophysical, geotectonic, and geochemical data for the Site and the methodology employed for the ESIA; and
- Assess the geochemical studies of Amulsar ores.

1.2.2 Assessment of the Impacts on Water Resources

Pursuant to the TOR, the main objectives of the review are to:

- Evaluate the potential impacts on water resources (surface water and groundwater) from various project activities during construction, operation, and post-closure; and
- Evaluate the proposed mitigation measures in the ESIA report for the Site.

The main concerns are potential impacts to:

- The Jermuk Springs, including the hydrothermal springs;
- The Spandaryan-Kechut tunnel and Kechut reservoir, which feeds Lake Sevan;
- Water supply sources for the seven communities within the vicinity of the mining facility;
- Various springs, especially those located on the flanks of the mine pits, near the Barren Rock Storage Facility (BRSF), and in vicinity of the Heap Leach Facility (HLF); and
- The Arpa, Darb, and Voratan Rivers.

Amulsar Gold Mine - Independent 3rd Party Assessment
Impacts on Water Resources, Geology, Biodiversity and Air Quality

July 22, 2019
3

The review entails assessment of the following items:

1. Lydian's evaluation of the existing hydrologic and hydrogeologic regime of the project area as part of the ESIA baseline assessment, including identification and hydraulic characterization of the subsurface and groundwater interaction with surface water; spring sources and emergence mechanisms; connections between various basins, especially with the Jermuk basin, and with the underlying deep aquifer system;

2. The adequacy of key groundwater data that were used in the assessment, including water isotopic, chemical, geochemical, and meteorological data, and surface water flow data;

3. The groundwater model developed for flow and contaminant transport predictions;

4. The water balance estimation for the prediction of surface water runoff;

5. The identification and characterization of potentially acid generating rock (PAG) and the assessment of the impacts of acid-rock drainage (ARD) on existing water resources; and

6. The adequacy of proposed environmental mitigation measures for the protection of water resources during normal operation and catastrophic events.

1.2.3 Assessment of the Impacts on Biodiversity

Pursuant to the TOR, the main objectives of the review are to:

- Understand and evaluate the impacts of the project on natural habitats and biodiversity;

- Conduct a due diligence study of the existing EIA to ascertain compliance with international standards on preservation and conservation of biodiversity;

- Evaluate the conservation status of patrimonial species (endemic, vulnerable, rare) including *Potentilla Acantholimon* and *Parnassius* among others; and

- Assess the measures proposed for reduction/avoidance of ecological impacts from the project.

1.2.4 Assessment of the Impacts on Air Quality

Pursuant to the TOR, the main objectives of the review are to:

- Review the adequateness of the data used to assess the air quality impacts;

- Evaluate the appropriateness of the ESIA/EIA assessment of the impacts from dust generation and its possible health effects taking into account where relevant the chemical composition of dust and the health impact on the surrounding community;

- Evaluate the appropriateness of the air dispersion modeling studies;

- Evaluate the adequacy of the mitigation measures proposed.

1.3 Bases and References

The assessment and conclusions in this report have been developed to a reasonable degree of scientific certainty based upon our review of:

- Relevant sections and appendices of the ESIA;
- English-translated sections of the EIA (provided in April-May 2019);
- Various ESIA model input data, technical memoranda, and studies prepared for the Site to assess impacts on water resources;
- Environmental monitoring reports and data;
- Relevant scientific reports from local experts;
- Published scientific articles and studies or information obtained via internet search;
- Data about the geology and water resources of the region provided by the MNP and ICRA;
- Amulsar Mine satellite geologic images;
- Lydian's responses to specific inquiries from ELARD-TRC Team and Lydian's comments on the June 14, 2019 Draft Report received via the ICRA;
- Relevant RA regulatory requirements; and
- Our knowledge of applicable requirements for similar sites, and standard practice guides.

Specific references that are cited in this report are listed in Section 5.0.

We understand the assessment may be limited because ELARD-TRC Team may have not been provided or may have not reviewed all the relevant information, data, and analyses. We reserve the right to amend our report and supplement our conclusions expressed herein as additional information becomes available.

1.4 Qualifications of Experts

- **Nidal Rabah**, PhD, PE, LSRP, PMP is a Vice President and the Director of Technical Development and Center of Research & Expertise (CORE) at TRC in New Jersey, USA. Dr. Rabah is a Licensed Professional Engineer, Licensed Site Remediation Professional, and Certified Projection Management Professional with more than 30 years of professional and academic experience with focus on advanced characterization, innovative remedial technologies, groundwater modeling, and water resources planning and development. He led numerous large-scale environmental assessments, remediation, and construction projects. He served on the Interstate Technical & Regulatory Counsel (ITRC) Remediation Management of Complex Sites Guidance team and authored and co-authored over 25 technical publications. He serves as a technical expert on environmental claims.

  He serves as a Technical Director and Lead Environmental Engineer on the assignment related to Water Resources and Geology.

- **David Hay**, PhD, CPG is a Principal Hydrogeologist and Geochemist at TRC in Colorado, USA. Dr. Hay is a Certified Professional Geologist with more than 30 years of experience with focus on hydrogeologic and hydrologic characterization and testing, geochemistry and geochemical modeling, groundwater flow and contaminant transport

modeling, mining characterization and remediation, and coal and oil/gas exploration and development. He was a member of the ITRC Guidance Teams for Characterization and Remediation of Fractured Rock and LNAPL. He has authored and coauthored over 20 technical papers and presentations. Dr. Hay is listed in TRC's national register of experts and is a member of several TRC CORE teams.

He serves as a Lead Hydrogeologist and Geochemist on this assignment.

- **Robert Stanforth**, PhD is a Senior Geochemist and Wastewater Treatment Expert at TRC in Wisconsin, USA. Dr. Stanforth has more than 30 years of professional and academic experience, with focus on hazardous waste treatment and environmental analysis. His areas of expertise include evaluating waste leaching characteristics, developing and applying treatment technologies for hazardous wastes and heavy metals, and developing and implementing wastewater treatment methods, and development and implementation of wastewater characterization analytical methods and laboratory treatability testing. He holds 11 patents on methods for treating hazardous waste and heavy metal leaching from soil or waste and has authored and presented over 60 technical papers. Dr. Stanforth is listed in TRC's national register of experts and is a member of TRC CORE teams.

  He serves as a Geochemist and Wastewater Treatment Specialist on the assignment related to Water Resources and Geology.

- **Ramez Kayal**, MSc is the President and a Principal Geologist/Hydrogeologist at ELARD Lebanon with more than 30 years of professional experience on conducting hydrogeological assessment, groundwater vulnerability studies, groundwater modeling as well as soil and groundwater remedial investigations. Mr. Kayal has extensive experience in working in mountainous regions and assessing impacts of projects on water resources.

  He serves as peer reviewer on the assignment related to Water Resources and Geology.

- **Carla Khater**, Ph.D., is a senior ecologist with more than 15 years of experience in ecosystem management and restoration ecology.

  She serves as a biodiversity expert and coordinator on the assignment related to Biodiversity.

- **Alexandre Cluchier** graduated from the French Sorbonne, Paris, and the University of Montpellier, in France; he is a Senior International Ecologist Expert and Advisor for project owners and governments with 20 years experience in biodiversity assessments as part of Environmental Impact Assessments for projects throughout Europe, Africa, the Middle East and the Caribbean area.

  He serves as a biodiversity expert on the assignment related to biodiversity.

- **Charbel Afif**, PhD is a Senior air quality expert. Dr. Afif has over 15 years of professional and academic experience. His areas of expertise include emissions estimation and treatment, measurements and metrology of air pollutants, design of air quality monitoring networks, air dispersion modeling, and design of air quality strategies. He has authored and coauthored over 70 technical papers and presentations.

  He serves as an Air Quality Expert and lead author of the assignment on Air Quality.

- **Ricardo Khoury**, ME. is a senior environmental specialist with more than 22 years of experience managing complex ESIA studies. He often supports international financing institutions, governments and project developers in developing bankable ESIA studies for projects in various sectors including mining, oil and gas, renewable energy, and public infrastructure among others.

  He serves as overall study coordinator and peer reviewer of biodiversity and air quality assignments.

1.5   Structure of the Report

This report is structured in a way to align with the Armenian Legislation related to such reports. It includes:

- An Introduction (Section 1)
- The Examination sub-divided in three sub-parts (Water and Geology, Biodiversity and Air Quality) (Section 2)
- Summary, Conclusions and Data Gaps (Section 3)
- Responses to Specific ToR questions (Section 4)
- References (Section 5)
- Appendices

2.0 Examination

2.1 Water and Geology

2.1.1 Baseline Characterization

Figure 4.1.4 of the ESIA (Wardell Armstrong, 2016) depicts the outline of the environmental baseline study area. In this report, this area is referred to as the Project Area as a general descriptor of the Amulsar Mine and vicinity.

2.1.1.1 Meteorological Data

Elevation strongly influences climatic conditions, including precipitation, temperature, and solar radiation. Elevation, therefore, is a key consideration in choosing a meteorological station for acquiring climate data. Other considerations are the period of record and completeness of data.

2.1.1.1.1 State

Two State meteorological stations are located near the Project Area. One station is in Jermuk, and the other station is on Vorotan Pass. The Vorotan Pass station is approximately 325 m higher than the Jermuk station. The mine pits are considerably closer to the Vorotan Pass station than Jermuk, and the elevations of the pits are closer to the Vorotan Pass station elevation than Jermuk (ESIA Table 4.2.1). The BRSF is 1 km closer to Jermuk than the Vorotan station, but the elevation of the BRSF is closer to the elevation of the Vorotan station. The elevation of the HLF is closer to the elevation at Jermuk, which is less than 1 km farther than the Vorotan station. These data suggest the Vorotan Pass station may have the most appropriate climate data for analyses related to the mine pits and the BRSF, and the Jermuk station data would be better suited for analyses concerning the HLF.

The Vorotan Pass station record is continuous for most measurements for 51 years, from 1962 to 2013. Use of these data are appropriate for all analyses, except potentially for the HLF analyses. Appendix 4.2.1 of the ESIA states that there are appreciable differences between the Vorotan Pass and Jermuk stations in the values of precipitation, evaporation, and temperature, as well as for snow depths and accumulation periods.

The Vorotan data were chosen for the baseline dataset. Section 4.2 of the ESIA states that the trends in Jermuk data are similar to Vorotan data. The period of record at Jermuk, however, is only 22 years, from 1992 to 2013. The Jermuk data were used for the updated Project Water Balance (Golder, 2018). Any other analyses for the HLF using Vorotan climate data are considered suspect.

2.1.1.1.2 Site

An on-site weather station, Capricorn-Columbia, is located on the southeastern edge of the BRSF. The period of record is short (2009 – 2011) and incomplete, but the data are purportedly comparable to the Vorotan Pass data.

2.1.1.1.3 Data Manipulation

The Vorotan Pass climate data were analyzed to develop an average climate year, extreme dry and extreme wet years, and typical dry and typical wet years (ESIA Tables 4.2.4 and 4.2.5). The average, extreme dry, and extreme wet years represent the statistical mean and the

corresponding minimums and maximums of precipitation and evaporation data. The typical dry and typical wet years, however, are based on a set of arbitrary assumptions. Rather than developing these so-called typical years, which are intended to produce a range of modeling results, a statistical approach is more defensible. For example, the 25th and 75th percentiles of precipitation and evaporation could be used in the modeling.

2.1.1.1.4 Climate Trends

Golder (2016c) made seasonal adjustments to the baseline climate information for the purpose of assessing the potential impacts that climate change may have on the results of evaluations using the baseline data. The adjustments are partly based on the 2014 projections for the Project region by the Intergovernmental Panel on Climate Change (IPCC) that used global climate models. The adjustments also reflect localized projections using a downscaled climate change model (UNDP Armenia), summarized in the Environmental and Social Impact Assessment for the Amulsar Gold Mine Project. The adjustments, which are relevant through 2030, are summarized in Golder (2016c Table 11). Temperature is adjusted for an increase of 1°C from September through February and 2°C from March through August. Precipitation is adjusted for a decrease of 11% from December through May, a decrease of 9% from June through August, and an increase of 5% from September through November. The adjustments have not yet been incorporated in any evaluations. Golder's (2018) updated Site-Wide Water Balance (SWWB), for example, is based on historical climate data.

Melkonyan and Gevorgyan (2017) analyzed historical climate data from numerous meteorological stations in Armenia for trends that may be indicative of future climatic conditions. Their results indicate that the Golder (2016c) adjustments in temperature and precipitation are consistent with trends for Armenia in general. However, the Melkonyan and Gevorgyan (2017) analyses for different elevations show that decreases in precipitation at elevations corresponding to the Project area are much less than Armenia in general (i.e., from 2,000-2,500m -0.8% and 2,500-3,000m -2.2%). They also concluded that climate risks and the frequency of hazardous hydrometeorological events have increased due to changes in the global atmospheric circulation.

2.1.1.2 Geology and ARD Geochemistry

2.1.1.2.1 Regional Setting

The regional geology is described in Section 4.6.1 of the ESIA. The Amulsar ore deposit is located in south-central Armenia in the Lesser Caucasus Mountains. The description of the regional geologic setting, including ore host rocks generated in a calc-alkaline magmatic arc system and the proximity of the Project Area to the suture zone associated with closure of the Neo-Tethyan Ocean, was verified by an independent literature search[1] (e.g., Adamia et al., 2011).

The description in Section 4.6.1 is brief, but sufficient, and includes a few regional geologic maps (ESIA Figures 4.6.1 and 4.6.2) that convey the essence of the tectonic setting. The information is also supported by documents provided by ICRA (Grosjean et al., 2018; Holcombe et al., 2013).

---

[1] The reference cited in the ESIA was unavailable.

Amulsar Gold Mine - Independent 3rd Party Assessment
Impacts on Water Resources, Geology, Biodiversity and Air Quality

July 22, 2019
9

2.1.1.2.2 Local Geologic Model

The description of the local geology in Section 4.6.2 of the ESIA is based on the work of Holcombe *et al.* (2013) and Holcombe (2013). The following summary of the local geology (excluding the Amulsar Tectonic Block) is a synthesis of key points from the original documents, augmented by relevant information from Oliver (2013), who contributed to an understanding of the sequence of events in the geologic history leading to ore deposition.

2.1.1.2.2.1 Rock Types, Stratigraphy, and Distribution

The Project Area is underlain by a very thick sequence of Paleogene volcano-sedimentary rocks. The rocks flanking the ore deposit consist of multiple fining-upward cycles of volcanogenic conglomerate and mass flow breccia, with marly mudstone and, locally, thin calcilutite limestone. The composition of the volcanic rocks is andesitic to dacitic. Some of the andesitic rocks are porphyritic and were interpreted to be intrusive (Oliver, 2013), as well as thick lava flows. The flanking strata are sub-horizontal to gently dipping and locally cut by steep faults. Scattered intermediate to silicic composition plutons and dikes occur in these rocks within and adjacent to the Project Area. At the lower elevations to the east and west of the Amulsar Mountain ridge and covering the northern face of the ridge, basalt lava flows post-date and overlie the Paleogene volcano-sedimentary and intrusive rocks, forming plateaus along the banks of the Vorotan and Arpa River gorges. Colluvium overlies the bedrock throughout much of the Project Area, with a thickness ranging from less than 1 m up to 20 m (ESIA Section 4.8)[2].

The Paleogene volcano-sedimentary rocks are subdivided into Upper Volcanics (VC/UC) and Lower Volcanics (LV). The VC and LV are described as follows (paraphrased from the ESIA):

- **VC:** Sparsely-bedded volcanogenic conglomerate, feldspathic sandstone, and minor siltstone which are interbedded with abundant thin and thick lenticular debris flows, minor andesitic lava flows, and volcanogenic/volcaniclastic breccia. Debris flows are dominated by pebble- and cobble-size breccia with sparse boulder-size components.

- **LV:** Dominantly feldspar-porphyritic andesite at high elevations, generally without flow characteristics, considered likely to have been intruded in the volcanic edifice. Subordinate rocks include feldspar and amphibole-porphyritic andesite, rocks with pebble- to cobble-size fragments, and indeterminate rock types. The volcano-sedimentary rocks described in the first paragraph of this sub-section crop out at lower elevations.

The VC crop out high on Amulsar Mountain and its eastern flank. Underlying the VC are extremely thick LV, which crop out all around Amulsar Mountain, extending from high elevations on the west side of the mountain to the gorge of the Arpa River. Noteworthy is the lumping of the porphyritic andesite with the LV. According to Oliver (2013), most of the porphyritic andesite post-dates deposition of both LV and VC.

2.1.1.2.2.1.1 Alteration

The gold deposit is associated with a zoned alteration largely controlled by rock type (Oliver, 2013). The distinguishing feature of the VC is pervasive silicification and strong alunite alteration. The silicification occurred preferentially in the volcaniclastic and clastic rocks. In

---

[2] Section 4.6.2 of the ESIA indicates the colluvium thickness ranges up to 30 m.

contrast, the LV is distinguished by pervasive argillic alteration in the region of the orebodies, grading to unaltered rocks with distance. Geoteam (2014) states that the argillic andesitic rocks are homogeneous and unbroken.

The ore deposit is interpreted to have evolved from a local volcanic edifice (Holcombe et al., 2013). Oliver (2013) interpreted a long history of silicification that may have begun prior to deposition of some of the volcaniclastic units. After sill intrusions of chemically distinct porphyritic andesite, further epithermal-style hydrothermal alteration occurred as proximal silicification, primarily affecting the VC, and distal, widespread quartz-sericite-pyrite (phyllic) alteration in the porphyritic andesite. Subsequently, with waning fluid temperatures, strong argillic and local alunite alteration occurred in the porphyritic andesite (overprinting phyllic alteration) and the LV, accompanied by local alunite and clay alteration in the upper volcanics around veinlets and contacts. Gold and hematite mineralization overprints all these alteration stages, and primarily occurs in the silicic VC. A late supergene weathering stage produced limonite and alteration of hematite to goethite.

2.1.1.2.2.2 Structure

The Amulsar gold deposit occurs within a ridge that is locally structurally-complex and purportedly surrounded by regionally simple structure characterized as sub-horizontal to gently dipping strata with little internal structure, except offsets produced by high-angle faults. Within the complex mineralized zone, the silicic VC is underlain by and interleaved with the argillically-altered LV and porphyritic andesite. Multiple stratiform panels of the clay-altered porphyritic andesite occur within the VC sequence, and these panels have complex fold geometries. Most of the andesite panels are believed to be intrusive sills, but the interleaving is at least partly structural (resulting from imbricate thrusting).

The silicic VC rocks and the argillic andesite panels only occur above a stratiform structural level called the basal contact. Below this contact, only argillic rocks were encountered during drilling, and the rocks immediately below the basal contact are the same porphyritic andesite as the interleaved panels. Above the basal contact, stacked sheets of the argillic porphyritic andesite have been locally observed with evidence of fault contacts (imbricate thrust faults). Locally, the thick lower andesite sheets and the basal contact are folded into a broad antiform.

The subdivision of the Paleogene volcano-sedimentary rocks into VC and LV derives from stratiform nature of the base of the VC. The basal contact has been referred to as a disconformity (e.g., ESIA Section 4.6.1), but the occurrence of the same argillic andesite above and below the contact negates this interpretation.

Prior to mineralization, an interpreted large overturned fold was breached by several thrust faults. Syn-mineralization deformation, including local thrust faulting and possibly dextral wrenching, refolded and offset older structures. The most prominent post-mineralization structures that overprint older structure are NE-trending normal faults that cross the ridge obliquely and delimit a series of horsts and grabens.

On the western side of the ridge, the lowest observed contact is a west-dipping, low-angle semi-ductile fault zone, with steeply dipping, locally folded VC rocks overlying the argillic LV rocks. This contact is believed to be an early northeast-directed thrust fault (Orontes Thrust). This structure was mapped through the horst block between Tigranes and Erato, and an east-dipping mylonitic zone on the eastern flank of the ridge is suggested to be structurally related.

Peripheral to the complex ridge structure, the structure is purportedly comparatively simple. Strata are sub-horizontal to gently dipping, and silica-altered VC rocks overly argillically-altered LV rocks. On the eastern side of Amulsar Mountain, the contact between the argillic LV rocks and the silicic VC rocks occurs at an undeformed stratiform contact (basal contact).

2.1.1.2.2.2.1   Amulsar Tectonic Block

The location and characteristics of the Amulsar Tectonic Block (ATB) are described in Geoteam (2014) and GRZ (2011). According to these documents, the Project Area is located in the ATB, a central autonomous tectonic block comprised of an Eocene-Oligocene volcanic dome, and the ATB is located in the interfluve area of the Arpa, Vorotan, and Darb Rivers. The ATB is triangular, bounded entirely by three major tectonic faults that intersect, the Kechut Fault, the Agarakadzor Fault, and the Zirak Fault.

The Geological Map of Vayots Dzor (Armenia) is included in the Geoteam (2014) document. Based on this map (includes fault traces), descriptions of the locations of the faults in GRZ (2011), and a physiographic map[3] showing the Mine and faults in the vicinity of the Project Area (Appendix A of this report), the faults were identified and labeled on the Geologic Map of Vayots Dzor (Appendix A of this report). Relevant descriptive information about the faults in GRZ (2011) are combined in the following paragraph with observations about the traces of the faults on the geologic and physiographic maps.

The Agarakadzor Fault is a major structural zone (up to 1 km wide) that intersects the Kechut Fault at or near the confluence of the Arpa and Darb Rivers and passes near and/or along the Darb River gorge to Vorotan Pass and is projected to intersect the Erato Pit, the Zirak fault, and the Vorotan River Valley. The Kechut Fault, one of the largest faults in the region, is a northeasterly striking structure (up to several hundred meters wide) that intersects the Agarakadzor Fault as noted and passes near and/or along the Arpa River Valley to Kechut Village and beyond. The Zirak Fault is oriented northwest-southeast, intersecting the Kechut Fault before passing beneath the Kechut Reservoir then through the Zirak Volcano, intersecting the Agarakadzor Fault, and passing beneath the Vorotan River. These three faults are visible and mapped on satellite imagery of SOYUZ 6 and ERTS-NASA. Hydrothermal alteration is associated with all three faults, structural deformation with the Kechut and Agarakadzor Faults, intrusive igneous rocks with the Kechut and Zirak Faults, and mineral springs with the Kechut Fault. According to Geoteam (2014), the Zirak Fault is clearly visible on the ground surface.

According to GRZ (2011) and Geoteam (2014), the ATB is autonomous (independent or isolated) due to its hydrogeological characteristics. They state that the ATB is not connected to adjacent regions, and the Mine cannot impact the hydrogeology and water quality, including mineral and fresh water springs, of the regions adjacent to the ATB, particularly the Jermuk mineral springs. Similar statements are included on the Lydian web page.

2.1.1.2.2.3   Mineralization

The Amulsar gold deposit does not conform to any simple type-classification (Oliver, 2013). The mineralization is most analogous to Chilean low-temperature, low-sulfur, iron oxide-copper-gold systems, which have alteration haloes similar to low to intermediate sulfidation epithermal systems. The deposit is structurally-controlled, oxidized, and low temperature hypogene, with a

---

[3] Included on web page of Lydian Armenia describing the mine and the ATB.

supergene overprint of limonite and goethite. The gold has a strong association with iron, copper, arsenic, antimony, bismuth, and lead, and is surrounded by, and largely overprints, a halo of variably phyllic-argillic-silicic altered volcanic rocks and intrusive porphyritic andesite. The structural association of gold is dominated by the infilling of faults and fractures and mosaic to chaotic breccias. Some of these breccias are fault-related hydrothermal breccias, but others show evidence for diatreme-like brecciation and coincident high-grade gold deposition. Quartz dominates the mineralogy of the ore occurrences, with hematite, limonite, and goethite, and minor rutile, chlorite, mica, alunite, and jarosite. A significant pre-history to the gold deposition includes the development of zoned alteration, largely controlled by rock type, with the earliest silicification probably occurring prior to the deposition of some of the volcaniclastic units.

2.1.1.2.2.4 Assessment of the ESIA Characterization of Local Geology

The geologic characterization work in the Project Area was focused on the high elevations of Amulsar Mountain in the vicinity of the ore deposits and the BRSF. The rest of the area bounded by the three rivers is only superficially described. Drawing 4.8.1 of the ESIA shows groundwater level monitoring locations for several other areas, where presumably subsurface geologic data were obtained, yet there are no cross-sections across the Project Area to depict the stratigraphy and structure. Cross-sections from the 3-D geologic model (Holcombe, 2013) only show the geologic relationships in the vicinity of the ridge (pits area). If geologic data are lacking for areas beyond the ridge or were obtained but not integrated into the conceptual model, this deficiency translates to poor understanding of the subsurface between sources and receptors of groundwater contaminants. For such an environmentally-sensitive area, the omission of illustrations of the structural and stratigraphic relationships across the Project Area is a serious shortcoming in the ESIA conceptual model. The conceptual geologic model is the basis for models that numerically represent groundwater flow and contaminant transport.

The ESIA description of the local geology is disorganized, incomplete, and incomprehensible without reading the original documents. The text gives the impression of poorly understood structural and stratigraphic relationships, distribution and causes of alteration types, and the sequence of events in the genesis and occurrence of the various rock types along the ridge. The text also seems unclear as to whether all the rock types and alteration types are characterized for ARD. One omission in the distinction and delineation of rock types is the widespread phyllic alteration. This phyllic alteration was apparently lumped with the argillic alteration, which is a local overprint on the earlier phyllic alteration. The text and illustrations, supported by the cited references, portray isolated complex structure of the ridge and geologic simplicity of the rest of the Project Area. This conceptualization is unrealistic given the occurrence of folds and thrusts on the ridge and the existence of bordering rivers that are structurally controlled.

The thrust and wrench faults mapped in the mineralized zone are manifestations of widespread crustal shortening related to collision of the Eurasian and Africa-Arabian lithospheric plates (Adamia et al., 2011). The faults are not limited to the ridge in the Project Area. The existence of the ridge and good exposure of structures may be partly due to the resistance of the silicic rocks to erosion. The imbrication identified on the ridge suggests structurally lower sub-parallel thrusts and folds occur in the Project Area. Holcombe (2013) suggested that the Orontes Thrust, the deepest low-angle structure identified on each side of the ridge and mapped through the horst block between Tigranes and Erato, is lying piggyback on another thrust fault at depth. High-angle faults mapped in the mineralized area also occur across the Project Area.

Detailed surface geologic mapping is lacking for the remainder of the Project Area. Faults are only delineated in the vicinity of the mineralization (ESIA Figures 4.6.3 and 4.6.7). One explanation for the absence of faults on surface geologic maps is that little effort was expended beyond the area of economic interest.

Faults may be barriers and/or conduits of groundwater flow. Furthermore, volcanic rocks are brittle, with widespread fracture permeability, including bedding-plane fractures. These characteristics influence groundwater flow and transport rates. The argillic rocks cannot be assumed to be a homogeneous clay zone, void of fractures. In fact, the processes associated with deposition of the ore superimposed brecciation on the altered rocks. Fracturing beyond the mineralized zone is not described in Section 4.6.2 of the ESIA or supporting documents on the geology, suggesting surface and borehole fracture characterization was not performed. The omissions of fault mapping and fracture characterization represent data deficiencies for conceptualization of the controls on groundwater flow paths and rock transmissivities. Correct numerical model representations of groundwater flow and solute transport from the pits and project facilities to receptors (rivers and springs) are dependent on the structure and characteristics of the rock throughout the flow and transport paths.

The Project Area is only partially encompassed by the ATB (Appendix A of this report). The entire Tigranes-Artavasdes-Arshak pit area and at least part of the Erato Pit are south of the Agarakadzor Fault and the ATB. Moreover, the BRSF straddles the trace of the Zirak Fault, with parts of the BRSF being north of the fault and the ATB. A large part of the Kechut Reservoir is within the ATB near its northern vertex. Potential seepage to groundwater from the part of the BRSF north of the Zirak Fault could result in contaminated groundwater reaching the Madikenc springs. Contaminated groundwater below the mine pits can flow to the Darb and Vorotan Rivers.

The locations of the Darb and Arpa Rivers are structurally controlled, and rivers are commonly hydraulic boundaries (no groundwater flow across the plane of vertical projection). Furthermore, faults may be barriers to groundwater flow, and the hydrothermal alteration increases the likelihood that the faults are barriers to groundwater flow. However, with part of the BRSF and most of the mine pit areas outside the ATB, it is incorrect to state that the mine cannot impact regions (including fresh water springs) adjacent to the ATB. Additionally, faults may be conduits of groundwater flow. Under such a setting, the Agarakadzor fault could conduct contaminated groundwater to the Darb and Arpa Rivers. Similarly, the Zirak Fault could conduct contaminated groundwater, including potential seepage from the BRSF (elevation approximately 2,600 m), to the Kechut Reservoir (elevation approximately 1,950 m) and/or the Vorotan River (elevation approximately 2,200 m at the projected intersection of the Zirak Fault).

Surface water and groundwater moving northward from the BRSF follow northwest trajectories toward the Arpa River and the Kechut Reservoir. Jermuk is at least 1,000 m higher than Kechut Reservoir. The Arpa River flows southward from Jermuk then southwestward from the Kechut Reservoir. The elevation of the river valley decreases to 1,400 m at the confluence of the Darb and Arpa Rivers. Groundwater potentials also decrease along the river valley in the direction of river flow. Furthermore, there is a northeast-oriented tributary to the Arpa River between Jermuk and the Mine facilities, which is a probable hydraulic boundary. Even with part of the BRSF being north of the Zirak Fault, seepage from the BRSF will not reach Jermuk. Finally, Jermuk is northwest of the trace of the Kechut fault, which may also be a barrier to groundwater flow.

2.1.1.2.3 ARD Potential - Acid Generation and Metals Leaching Potentials

Sources of potential environmental impacts related to the geology of the Project include pit walls, adits, barren waste rock (including pit backfill), a low-grade ore stockpile, and spent ore in the heap leach pile. Section 4.6.5 and Appendix 4.6.2 (GRE, 2014d) of the ESIA summarize the ARD characterization for the Project. Characterization of the potentials for ARD, leaching of metals, and generation of other constituents of concern (COCs) was performed for two basic rock types, VC and LV, and colluvium. Subsequently, an ARD block model was developed (GRE, 2018b) to determine the quantity and distribution of potentially acid generating (AP) waste rock.

Figures 4-1 and 4-2 of Appendix 4.6.2 of the ESIA show the distribution and density of sampling in the Tigranes/Artavasdes and Erato pit areas, respectfully. Table 4-1 of Appendix 4.6.2 (GRE, 2014d) shows the types and numbers of characterization tests performed on barren rock and spent ore from each pit area and borrow materials. The characterization tests are acid-base accounting (ABA), net acid generation (NAG) pH, bulk chemistry, mineralogy, synthetic precipitation leaching procedure (SPLP), NAG effluent, and humidity cell (HC).

2.1.1.2.3.1   Characterization Methods

Extensive characterization should be performed for each geochemical test unit. Geochemical test units are rock types of distinctive lithology, mineralogy, and/or alteration (e.g., Maest et al., 2005). The units should be as homogeneous as possible based on lithology, mineralogy, alteration, and the extent of exposure of minerals to weathering. Depending on the results of the characterization, some of the test units may be combined, or it may be necessary to subdivide them for waste management purposes.

2.1.1.2.3.1.1   Mineralogical Analyses

Mineralogical data are an essential component of ARD characterization because the mineralogical properties determine the physical and geochemical stability and reaction rates of geologic materials and mine wastes (e.g., INAP, 2009). The types of mineral phases indicate the major chemical constituents and relative reaction rates. Surface exposure, grain size, and deformities also affect reaction rates. One of the most important uses of mineralogical data is support for and design of other tests and interpretation of the results. Mineralogical analysis is typically required for a representative sub-set of the static test samples and each kinetic test sample. Mineralogical data indicate which minerals likely contributed to test results and the likelihood they will contribute similarly in the natural environment. Representative samples are based on a good understanding of the geology and geochemical variability (e.g., alteration types) from previous analytical work related to exploration. At a minimum, visual identification of minerals in core, petrographic analysis (transmitted and reflected light), and X-ray diffraction (XRD) should be performed.

Whole Rock Geochemistry

Whole rock analysis (bulk chemistry) determines the total concentrations of constituents in a rock sample. These data assist in identifying constituents of concern, but they are not a measure of potential concentrations in ARD. Elemental analysis methods include inductively-coupled plasma (ICP), atomic absorption spectroscopy (AAS), and X-ray fluorescence (XRF).

Static Testing

Two basic types of tests are available for determination of ARD potential: 1) ABA determines the net acid potential or net acid consuming capacity through independent measurements of

maximum potential acidity (AP) and acid neutralizing capacity (NP), and 2) the NAG procedure, which yields a pH that is indicative of the likelihood of net acid generation and the amount of acid generated in the test (e.g., Stewart et al., 2006).

ABA test results are used to calculate the net potential ratio (NPR) and net neutralization potential (NNP):

$$NPR = NP/AP$$
$$NNP = NP - AP \ (TCaCO_3/kT)$$

Table 4.7.4 in Section 4.7.1 of the ESIA shows screening guidelines for ARD potential. A sample is potentially net acid generating (PAG) with NPR < 1, non-PAG with NPR > 2, and uncertain with NPR ranging from 1 and 2 (INAP, 2009). PAG has been defined for NNP < -20, non-PAG for NNP > 20, and uncertain for NNP ranging from -20 to 20. Use of NNP is not recommended for characterizing ARD potential (INAP, 2009) because NNP is additive and must be greater than zero for NPR >1.

Site-specific NPR values have been developed in some countries and are law (regulatory criteria) in some states in the USA. At some Australasian sites, NPR > 3 is used as a conservative threshold between PAG and non-PAG. The State of New Mexico has a regulated NPR value of 3 for non-PAG, and an NPR threshold of 1.2 is law in Nevada.

The NAG test is used in conjunction with ABA to classify the acid generating potential of a sample (Stewart et al., 2006). A NAG pH < 4.5 indicates the sample is PAG. NPR = 1.0 separates PAG from non-PAG. A plot of NPR vs NAG pH identifies a PAG quadrant, a non-PAG quadrant, and two uncertain quadrants (INAP, 2009). Samples with conflicting ABA and NAG pH results plot in the uncertain quadrants. These samples require further test work. Sub-classification of PAG as low capacity and high capacity is also informative, which is based on the amount of acidity determined by titration to pH 4.5 (Miller, 1998). Also, sequential NAG tests should be performed on samples with pyritic sulfur contents greater than 0.7% to determine the total acidity due to incomplete oxidation of sulfide sulfur (resulting from peroxide decomposition effects).

ABA and NAG tests are inexpensive and should be applied to a large number of samples. The results are used for identifying samples requiring additional testing to better characterize ARD potential and may provide operational screening criteria for mine waste classification and management. ABA should always be conducted. The NAG test may be omitted for samples with very little sulfur or for samples with significant excess NP based on ABA test results.

Kinetic Testing

Laboratory kinetic tests are used to validate and interpret static test results and predict long-term weathering rates, ARD potential, and mine water chemistry. Both acid generation and metals leaching can be evaluated with kinetic testing. Various types and procedures of kinetic testing all involve subjecting samples to periodic leaching and analyzing the leachate. The test materials must be characterized before testing begins.

The two laboratory kinetic tests generally used are HC and column tests. HC tests are ASTM standardized tests (ASTM, 2007) conducted under fully oxygenated conditions with periodic flushing of reaction products. Information derived from the tests includes weathering rates of

sulfides and dissolution rates of readily soluble primary and secondary minerals. A common endpoint for HC tests is demonstrated time-constant values of leachate parameters.

Standards do not exist for column tests, which can simulate a variety of conditions. Column tests permit precipitation of secondary minerals from constituents leached from primary minerals, providing a better assessment of drainage chemistry. Column tests may simulate site-specific conditions and mitigation measures such as covers and amended mine wastes.

Leach and Effluent Tests

The SPLP is one of several short-term leach tests that measure readily soluble constituents in mine wastes (e.g., Maest et al., 2005). The test simulates the effects of short-term interaction of materials with rain and snowmelt, but it provides no information on long-term leach rates.

The effluent from NAG testing can be analyzed to provide an assessment of the effects of long-term weathering on mine water chemistry. Karlsson and Kauppila (2016) found that analysis of NAG leachate provides a reasonable estimate of metals concentrations for pH < 4 and that the NAG leachate at least indicates elements that are likely to be elevated at higher pH.

Field methods may be used to most realistically evaluate the potential for ARD and metals leaching. The methods range from rock wall washing to test piles of large quantities of materials (INAP, 2009). The advantages of field methods are assessment under ambient site conditions, including seasonal effects, and evaluation of the effects of discrete events such as intense storms or snowmelt. Monitoring leachate water quality related to historic mining activities (e.g., waste rock piles and adits) can provide using information about weathering rates and water quality under ambient conditions.

2.1.1.2.3.2 Assessment of the ESIA Characterization of ARD Potential

The distributions of sample locations for ARD assessment are reasonable for both pit areas. However, the sample categories of VC and LV reveal little about specific mineralogic and rock characteristics of each sample. There are significant variations in each category.

Within the two basic rock types (VC and LV), alteration sub-types may include silica VC, silica-alunite VC, argillic LV, argillic-alunite LV, silica-sericite-clay LV, phyllic LV, and other rock sub-types, including unaltered LV. Ore may be considered a sub-type primarily of VC. Ore occurrences include hematite and gossanous hydraulic breccias and veins in faults and fractures. Colluvium is a waste type derived from VC and LV with variable grain size and composition that also requires characterization. Multiple representative samples of each rock sub-type, ore occurrence, and sediment in each of the various pit areas require characterization. Spent ore characterization should include breccia and vein types. Mineralogical analyses of each rock sub-type, ore occurrence, and sediment may reveal additional or fewer divisions based on distinct mineral assemblages, including secondary minerals, with the ultimate objective of defining geochemical test units (Maest et al., 2005).

Mineralogical analyses were performed by XRD and transmitted and reflected light microscopy on 8 samples of Tigranes/Artavazdes and 12 samples from the Erato pit areas (Appendix 8.1.9). Only 5 LV and 3 VC samples were analyzed from the Tigranes/Artavazdes pit area, and only 5 LV, 4 VC, and 3 colluvium samples from the Erato pit area. The number of samples is insufficient for each category, and the choice of samples was not based on sub-types of VC and LV. There is no way to know whether all rock sub-types are represented for VC and LV or whether the set of mineralogic analyses for each category is representative of the range

geochemical variability and whether a mineralogic analysis is representative of any particular rock sub-type. The lack of correlation between rock sub-types and mineralogic data has repercussions for all other testing.

Based on existing mineralogical analyses, the important minerals include quartz, feldspars, sericite, illite, kaolinite, alunite, jarosite, pyrite, hematite, limonite, and goethite. Tables 4.6.2 and 4.6.3 of the ESIA and Table 9 of Appendix 8.19 (GRE, 2017), summarizing the mineralogic data for VC and LV, reveal significant variations in the mineralogy of the samples in each category which demonstrate the need for rock sub-types. Mineralogic analyses were not performed on the ore, but even composites of the ore reveal significant differences in whole rock analyses (ESIA Table 4.6.1) indicative of mineralogic differences. No mineralogic analyses were performed on colluvium in the Tigranes/Artavazdes pit area and no analyses were performed on borrow materials.

A significant number of whole rock analyses were performed for barren rock in each pit area (Appendix 4.6.2 Table 4-1), but the vast majority of analyses were just total metals. Based on Appendix 4.6.2 Table B-4, the only major element analyses that were performed are for the Tigranes/Artavazdes pit area, where only 6 analyses were performed for LV and 3 for VC. There are no analyses of Tigranes/Artavazdes spent ore. Unfortunately, none of the results can be related to rock sub-types with characteristic mineralogy and, and the results cannot be used to assess whether one particular sub-type suggests greater risk than another, which would be useful in selecting samples for other tests.

For the barren rock in the Tigranes/Artavazdes pit area, 154 ABA tests were performed without any NAG pH tests to complete the classification. Likewise, for the spent ore of this pit area, 6 ABA tests were conducted without complementary NAG pH tests. For the barren rock of the Erato pit area, 80 ABA tests were performed and only 50 NAG pH tests. State-of-the-art ARD characterization requires both ABA and NAG pH tests to classify the samples (It is noted that a plot of NPR vs. NAG pH for samples with both tests is included in Appendix 4.6.2), unless the samples have very little sulfur, or the ABA results indicate significant excess NP. The rocks have very little NP, and significant excess AP in the LV. At a minimum, all LV samples should have had the NAG pH test performed. Justification for omitting this test for the VC samples based on the amount of sulfur would be appropriate. Titration is a standard part of the NAG pH test (Stewart *et al.*, 2006), and the data on the amount of acidity should have been used to further classify the sample, with sequential NAG tests for the many samples with pyritic sulfur contents greater than 0.7% (Appendix 4.6.2 Tables A-1 and A-2). None of the existing static test results can be related to rock sub-types with a characteristic mineral assemblage for interpretation of test results.

Noteworthy is that the Modified Sobek method was used for the Project ABA, which determines AP based only on sulfide sulfur. This approach is clearly incorrect for the Project because nearly all samples from both pit areas have acidic paste pH values (Appendix 4.6.2 Tables A-1 and A-2), indicative of acidic sulfate salts (e.g., alunite and jarosite), identified in both VC and LV. The analyzed percentage of sulfate should have been included in the AP calculation (INAP, 2009), which would have resulted in lower NPR values. Negative values of NPR (impossible) and units of $TCaCO_3/kt$ (NPR is a unitless ratio) are reported in Tables A-1 and A-2.

HC tests were performed on only 8 barren rock samples from the Tigranes/Artavazdes pit area. No HC tests were performed for the Erato pit area. This data set is inadequate to cover the

Amulsar Gold Mine - Independent 3rd Party Assessment
Impacts on Water Resources, Geology, Biodiversity and Air Quality

July 22, 2019
18

range of rock sub-types with uncertain status based on static test characterization, especially with incorrectly calculated AP and the potential for some VC rocks to be acid generating (see below). None of the HC test results can be related to rock sub-types with a characteristic mineral assemblage for interpretation of test results.

The main concern with the SPLP testing is whether the range of rocks with secondary minerals were tested without defined geochemical test units. Similarly, NAG effluent results cannot be correlated with characteristic mineral assemblages for interpretation of results. Noteworthy is the lack of NAG effluent testing for Tigranes/Artavazdes spent ore.

Section 4.6.5 of the ESIA states that the VC is not acid generating. Appendix 4.6.2 Tables A-1 and A-2 show that there are many VC samples with significant pyritic sulfur, more than double the cited "low total sulfide (around 0.15%)", ranging to more than 5% in the extreme in both pit areas. Although these samples are a minority among the VC samples, the higher sulfide percentages provide more evidence that the VC is not homogeneous and should be sub-divided into distinct rock sub-types (geochemical test units).

Section 4.7.5 of the ESIA suggests that the HC tests would be conducted for up to a year. Four of the tests were terminated at 20 weeks. VC samples ARD-78C and ARD-80C appear to have not been given sufficient time to determine final pH based on the plots of other samples with longer test periods. The other two 20-week tests attained low and stable pH, but other parameters were not stable, including acidity, conductivity, sulfate, iron, and aluminum.

It cannot be concluded that the ARD potential of the VC does not translate into ARD generation. Two of the HC tests on VC were terminated prematurely. The three tested samples have low pyritic sulfur percentages (<0.01, 0.06, and 0.08). There are VC rocks with much higher percentages of sulfide that were not tested.

The three LV HC samples that generated no significant sulfate or iron have low pyritic sulfur percentages (0.2, 0.3, and 0.8). The other two LV samples that generated pH below 3 and high iron and sulfate have pyritic sulfur percentages of 2.1 and 4.2 percent. Many (29) LV samples (24%) in Appendix 4.6.2 Tables A-1 and A-2 have more than 2% pyritic sulfur, and 39 of 121 LV samples (32%) have significant pyritic sulfur (>0.7%). Therefore, the insignificant solute concentrations of the three LV samples must not be emphasized (as implied in Section 4.7.7 of the ESIA). Furthermore, based on the interpreted role of ferric iron in oxidation of pyrite in sample ARD-74C, the 24 % of LV with more than 2% pyritic sulfur may be expected to behave similarly.

Section 4.7.10 of the ESIA states that three of the five LV kinetic cells showed strong resistance to pyrite oxidation by ferric iron and that these samples produced consistently mild pH (greater than 4.5) with low sulfate and iron concentrations despite long-duration testing. These three samples have the low pyritic sulfur percentages (0.2, 0.3, and 0.8), which could not produce enough acidity to drive the pH below 3.5, where significant dissolved ferric iron concentrations greatly increase the rate of sulfide oxidation (INAP, 2009).

The leachate from the Site 27 Soviet era waste pile has a pH of 3.3 and high acidity. These data are a reasonable indicator of the potential of the ARD from the Amulsar Mine.

GRE initiated an on-site bucket kinetic testing program in 2017 (GRE, 2018a). The program included seventeen buckets filled with LV rock and three buckets filled with VC rock. The buckets are filled to 20-liter capacity and exposed to natural conditions. The LV sample selection was skewed toward samples with expected acidic properties. The range of pyritic sulfur of the LV samples is 0.04% to 9.48% (5 samples with <0.1% and 11 samples with >4.0%). Pyritic sulfur for the VC ranges from 0.07% to 0.13%.

GRE (2018a) stresses the bias in testing high pyritic sulfur samples. According to GRE, the ARD block model shows that only approximately 15% of LV is high AP waste. Minor high pyritic sulfide VC types were not subjected to bucket testing.

The rock was obtained from old core boxes with drilling dates generally ranging from 2010 – 2012 and one box with 2007 core. Pictures of the buckets reveal cobble-size material. ABA analyses were obtained for all test samples. ABA analyses were also performed on an additional 21 samples considered waste rock (8 VC and 13 LV).

ARD suppression tests are also being performed on high pyritic sulfur samples to determine the best amendment. In June 2018, six of the 20 bucket tests were converted to suppression tests.

The bucket testing was initiated October 2017 (GRE, 2018a). Noteworthy is the application of an initial rinse in November 2017 without leachate collection. The first leachate collection occurred December 2017 followed by four collections in May and June 2018 (date of memo is July 2, 2018). Field parameter measurements are pH, oxidation-reduction potential, conductivity, and dissolved oxygen. The December 2017 measurements show low pH (< 3.5) in 11 of the LV samples, with conductivities (μS/cm) ranging from over 1,000 to +/- 10,000. The pH of the other LV samples ranges from 4.5 to 6.0 (variable for each sample). One of the VC samples attained a pH as low as 4.0 in May 2018, and the other two VC samples generally show pH ranges from 4.5 to 6.0 (variable for each sample). Conductivities of the VC and many of the LV were in the range of 100.

A generally good correspondence is observed between ABA and bucket test results, with the 11 LV samples having pyritic sulfur greater than 4% producing pH less than 4. The one LV sample with 1% pyritic sulfur produced pH between 5 and 6 with a downward trend in May and June. The lower pyritic sulfur percentages produced the higher pH range of 4.5 to 6.0. The VC sample that produced pH as low as 4.0 (4.6 – 5.75 in May and June) has 0.13% pyritic sulfur. These results reinforce the need for sub-types of rocks (geochemical test units) and that VC has potential for acid generation even at the lower end of the pyritic sulfur range (0.13%) identified in the original ABA testing (up to and more than 5%).

GRE (2018a) stated that due to the drilling schedule, there was no fresh rock available for testing, necessitating using old core rock. Furthermore, GRE (2018a) stated that the high AP rock had oxidized in the core boxes, the objective of determining how fast the rock generates acid was not met, and that it will be necessary to redo the experiment. The oxidation observed in the core boxes, however, provides an indication of the rapidity of acid generation (with respect to drilling dates). The ramifications of the initial rinse in November 2017, as well as parameters of the leachate, are unknown. Considerable release of stored acidity in secondary minerals is probable. Measurement results in May and June 2018 display a slow, very minor increase in pH for nine samples. Minor to moderate decrease in conductivity is also recorded. Unclear is how much additional oxidation occurred between December 2017 and May 2018 and whether the increase in pH of these samples in May and June represents continued dissolution

Amulsar Gold Mine - Independent 3rd Party Assessment
Impacts on Water Resources, Geology, Biodiversity and Air Quality

July 22, 2019
20

of residual secondary minerals or continued pyrite oxidation accompanied by a decrease in exposed surface area.

The results of the entire characterization program should be viewed with caution. Although all the basic types of characterization were performed, there appears to be little planning and continuity in the approach.

Noteworthy is the recent development of the ARD block model (GRE, 2018b), which incorporates subdivision of LV based on the percentage of total sulfur. Previously, all LV was assumed to be PAG and managed the same. The model is generally based on the conservative assumption that total sulfur is a proxy for sulfide sulfur and that total sulfur greater than 2 percent is strongly acid generating (SAG). This approach improves ARD management of the LV rock but does not rectify the deficiencies in characterization described above.

The block model only subdivides the LV. All VC is still considered non-PAG rock. The conclusion that the ABA data histogram (GRE, 2018b Figure 1) "confirms" some LV samples were "incorrectly logged" as VC or that "some VC samples have very high sulfate sulfur" is suspect. Even if the high total sulfur is sulfate sulfur in VC rocks, which is not necessarily correct (can also be sulfides in VC), the block model excludes these samples (because they are purportedly sulfates and VC).

A coordinated effort should have been employed for the characterization, beginning with careful macro-identification of rock types based on exploration core for potential definition of geochemical test units. This step would be followed by petrographic and XRD analyses to confirm distinctive lithology, texture, mineralogy, and alteration. Geochemical characterization of the potential test units can confirm, reduce, or expand the number of geochemical test units. Volumes of each test unit are estimated, and an appropriate number of samples is determined. The samples for each geochemical test unit are then subjected to the full range of geochemical tests (except HC), with mineralogic data for each test unit. The final step of characterization is kinetic testing on a representative number of samples from each geochemical test unit, with emphasis on rocks classified as uncertain by the static testing. Mineralogy of the kinetic test samples is important.

The ARD with pH in the range of 4 – 5 cannot be dismissed. Acid contributes to the rate of chemical weathering of rock, which can accelerate physical weathering. Accelerated weathering contributes to the rate of exposure of more pyrite in all rock types at Amulsar. With enough pyrite exposed, very low pH solutions develop that mobilize metals, as observed in the HC tests.

2.1.1.2.3.3   Assessment of ARD Geochemistry

2.1.1.2.3.3.1   Geochemical Reactions

The ARD Management Plan (GRE, 2017 Section 3.9.1) states the following about ARD reactions:

> The kinetics of an ARD reaction are critical in defining the environmental impacts. Two different chemical reactions typically form ARD from the oxidation of pyrite. Equation 1 involves the oxidation of pyrite in the presence of water:
>
> $FeS_2 + 7/2O_2 + H_2O = Fe^{2+} + 2SO_4^{2-} + 2H^+$ [1] (INAP, 2009)
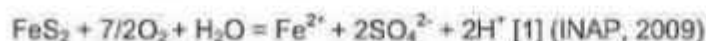
This reaction commonly occurs in LV material tested at the Amulsar site. However, in the kinetic cells, a second reaction dominated the ARD behavior of some cells later in the testing period. This equation involves the oxidation of pyrite by ferric iron (Fe^{3+}). This reaction is much faster and has a higher stoichiometric ratio between pyrite and acidity (listed as H+).

$$FeS_2 + 14Fe^{3+} + 8H_2O = 15Fe^{2+} + 2SO_4^{2-} + 16H^+ \quad [2] \text{ (INAP, 2009)}$$

Equation 2 is catalyzed by the bacteria thiobacillus ferroxidans [*sic*][4]. In subsequent sections, the changeover from ARD dominated by Equation 1 to ARD dominated by Equation 2 is referred to as: "ferric iron oxidation" because ferric iron is acting as a reactant in the oxidation of pyrite.

The statement that two reactions are responsible for acidity from pyrite (FeS_2) is incorrect. GRE (2017; Section 3.9.1) disregards the roles of ferrous iron oxidation and ferric hydroxide generation (or hydrolyzed ferric iron) as steps in the generation of acid. Based on GRE (2017), all the acid in the reaction sequence in Section 3.9.1 comes from the oxidation of sulfi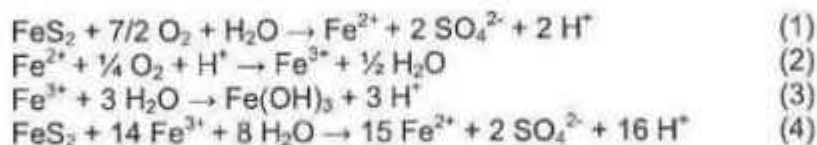de to sulfate, with dissolved ferrous iron (Fe^{2+}) as a reaction product remaining in solution. The discussion in Section 3.9.1 (GRE, 2017) is based on the ARD section of GARD Guide (INAP, 2009). The GARD Guide discussion, in turn, is based on a discussion of pyrite oxidation by Stumm and Morgan (1981), wherein the reactions are presented in a different sequence:

$$FeS_2 + 7/2\,O_2 + H_2O \rightarrow Fe^{2+} + 2\,SO_4^{2-} + 2\,H^+ \qquad (1)$$
$$Fe^{2+} + \tfrac{1}{4}\,O_2 + H^+ \rightarrow Fe^{3+} + \tfrac{1}{2}\,H_2O \qquad (2)$$
$$Fe^{3+} + 3\,H_2O \rightarrow Fe(OH)_3 + 3\,H^+ \qquad (3)$$
$$FeS_2 + 14\,Fe^{3+} + 8\,H_2O \rightarrow 15\,Fe^{2+} + 2\,SO_4^{2-} + 16\,H^+ \qquad (4)$$

Reactions 1 and 2 to 3 above are the primary contributors to acidity in pyrite oxidation. The GARD Guide reverses the order in which the reactions are presented, so that the ferrous iron oxidation is presented as Reaction 3, which is simply stylistic. However, GRE (2017) leaves out the ferrous iron oxidation reaction altogether, and in doing so leaves out half of the acid generating reactions in ARD. This significant oversight brings into question Lydian's assessment of acid generating potential of the rock and of the water quality in the ARD.

The oxidation of pyrite by ferric iron, Reaction 4 in the Stumm and Morgan (1981) sequence, only occurs after pyrite oxidation has been well established and significant acidity generated, because the ferric iron involved in Reaction 4 is only soluble and available under low pH conditions. The reaction between ferric iron and pyrite is much faster than the reaction between pyrite and oxygen and Reaction 4 will dominate if there is much dissolved ferric iron. Williamson *et al.* (2006) suggest that the reaction between ferric iron and pyrite dominates at a pH below about 3.2, with oxygen being the dominant reactant with pyrite above that pH level. The GARD Guide (INAP 2009 Figure 2-16) indicates Reaction 4 occurs at pH levels below approximately 3.2. The first three reactions in the Stumm and Morgan (1981) sequence are the primary acid-generating reactions. Because the dissolved ferric iron in Reaction 4 is a result of pyrite oxidation in the first place, the reaction does not generate any more acid per mole of pyrite than do the first three reactions. Note that once formed, ferric iron can generate acid either from hydrolysis and precipitation as hydrous ferric oxide (Reaction 3) or by reacting with additional pyrite (Reaction 4).

---

[4] *Thiobacillus Ferrooxidans*

GRE (2017) places emphasis on the reaction between ferric iron and FeS_2 ("*ferric iron oxidation*"), so it is instructive to examine Reaction 4 further. Presumably, pyrite oxidation is the original source of the dissolved iron and sulfate. The ferric iron is generated from the oxidation of the ferrous iron released by pyrite oxidation. Once ferric iron reaches a sufficient concentration in solution as the pH decreases, it will then start reacting with additional pyrite.

We can combine the reactions for the original reaction between pyrite and oxygen (Reaction 1), the reaction between ferrous iron and oxygen to generate ferric iron (Reaction 2), and the reaction between ferric iron and pyrite (Reaction 4) to generate an overall reaction for pyrite oxidation by ferric iron, as shown below:
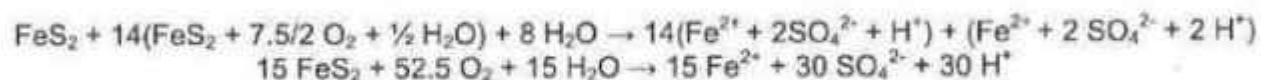
Reaction of oxygen with pyrite and ferrous iron:

$$FeS_2 + 7/2\ O_2 + H_2O \rightarrow Fe^{2+} + 2\ SO_4^{2-} + 2\ H^+ \quad (1)$$
$$Fe^{2+} + \tfrac{1}{4}\ O_2 + H^+ \rightarrow Fe^{3+} + \tfrac{1}{2}\ H_2O \quad (2)$$
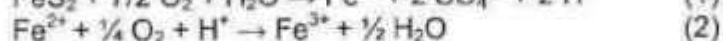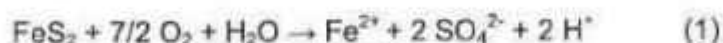
Combining these reactions:

$$FeS_2 + 7.5/2\ O_2 + \tfrac{1}{2}\ H_2O \rightarrow Fe^{3+} + 2\ SO_4^{2-} + H^+$$

We need 14 Fe^{3+} to oxidize pyrite, so the equation to oxidize pyrite by Fe^{3+} becomes:

$$FeS_2 + 14(FeS_2 + 7.5/2\ O_2 + \tfrac{1}{2}\ H_2O) + 8\ H_2O \rightarrow 14(Fe^{2+} + 2SO_4^{2-} + H^+) + (Fe^{2+} + 2\ SO_4^{2-} + 2\ H^+)$$
$$15\ FeS_2 + 52.5\ O_2 + 15\ H_2O \rightarrow 15\ Fe^{2+} + 30\ SO_4^{2-} + 30\ H^+$$

Simplifying, gives:

$$FeS_2 + 3.5\ O_2 + H_2O \rightarrow Fe^{2+} + 2\ SO_4^{2-} + 2\ H^+$$

This combined equation is identical to Reaction 1. Therefore, the overall reaction between pyrite and ferric iron is the same as the reaction between pyrite and oxygen. The reaction with ferric iron is faster, with the ferric iron acting as a catalyst, but the overall stoichiometry is the same. The original oxidant is oxygen. The sulfate to ferrous iron ratio is 2:1 at the end of the reaction. The predominance of one reaction over another reaction cannot be determined from the final concentrations of iron and sulfate or the final pH.

Both the iron and sulfur in pyrite contribute to acidity. The sulfur contributes in the first step of pyrite oxidation (Reaction 1). However, once sulfur is oxidized and sulfate is generated, sulfur does not contribute further to acidity. Ferrous iron contributes acidity as it oxidizes to ferric iron and then hydrolyzes[5] or precipitates as ferric hydroxide[6]. Whereas acidity from sulfide oxidation is generated directly (Reaction 1), the acidity from ferrous iron is generated after iron is oxidized.

The reaction between pyrite and ferric iron (Reaction 4 in Stumm and Morgan (1981)) is abiotic. Reaction 2 (ferrous iron oxidation) is slow at acidic pH values, but it can be catalyzed by

---

[5] $Fe^{3+} + H_2O \rightarrow Fe(OH)^{2+} + H^+$
[6] $Fe^{3+} + 3H_2O \rightarrow Fe(OH)_3 + 3H^+$

bacteria[7]. Both Reactions 1 and 2 are slow when abiotic, so the bacteria-catalyzed oxidation greatly enhances the rate at which ARD occurs.

The ferrous iron can be transported in the ARD-impacted water until the water is oxygenated and the iron is oxidized. These processes can occur at some distance from the location of pyrite oxidization (e.g., where groundwater with ferrous iron in solution discharges to a stream).

Ferric iron can precipitate as hydrous ferric oxide and generate acid, as shown by Reaction 3. Ferric iron can also precipitate as transient ferric hydroxy sulfates such as jarosite ($KFe_3(OH)_6(SO_4)_2$) or schwertmannite ($Fe_8O_8(OH)_6(SO_4)$) that make up part of the "yellow boy" characteristic of ARD. These minerals serve as stable reservoirs of stored acidity (Madden et al., 2012; Stahl, et al., 1993; Welch et al., 2008) at low pH. At pH values above about 3 (jarosite) to 4 (schwertmannite), these minerals dissolve incongruently to hydrous ferric oxides, sulfate, and acid. Jarosite has been identified in the rocks at the site. The reaction for dissolution of jarosite is shown below:

$$KFe_3(OH)_6(SO_4)_2 + 3H_2O \rightarrow K^+ + 3\ Fe(OH)_3 + 2\ SO^{2-} + 3H^+$$
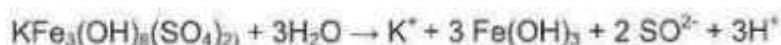
In this incongruent dissolution reaction, the iron remains in the mineral (solid) phase and potassium, sulfate, and acid are released to solution. Thus, after the products of the initial pyrite oxidation have been transported away in surface water or groundwater and precipitated as secondary minerals, water chemistry may be influenced by jarosite or schwertmannite dissolution, with little iron in the water (Smith et al., 2005).

Aluminum minerals in soil or rock can neutralize the acid from pyrite oxidation, yielding dissolved aluminum (Al^{3+}), which behaves as a less acidic version of ferric iron. The dissolved aluminum can precipitate as secondary minerals such as alunite ($KAl_3(OH)_6(SO_4)_2$), which is also found at the Site as part of the hydrothermal alteration mineral assemblage. Aluminum precipitates as a hydroxide at a higher pH than ferric iron (Snoeyink and Jenkins, 1980) generating acid, but the pH is buffered at a higher value than the reaction for precipitation of hydrous ferric oxide. Like jarosite, alunite is stable in acidic environments and dissolves incongruently to produce gibbsite at pH above about 4.5 (Reuss and Johnson, 1986).

The iron minerals jarosite and schwertmannite are associated with acidic, iron-rich environments such as ARD and are not stable in neutral environments. These minerals are transient phases that precipitate as a result of pyrite oxidation. The widespread occurrence of jarosite in the rocks at the Site indicates that pyrite oxidation has been occurring without mining activities and highlights the potential for much greater ARD generation after mining. GRE (2017) does not discuss the contribution of jarosite to ARD.

The GRE (2017) discussion of pyrite oxidation neglects half of the acid-generating reactions (Reactions 2 and 3) and thereby underestimates the potential ARD loading of the waters at the Site (for pH > 3.2) and the treatment needed to mitigate the corresponding impacts. The ARD mitigation and treatment plan presented in GRE (2017) may prove insufficient to treat the ARD. The ferrous iron oxidation is an important process to consider because additional acidity can be

---

[7] Bacteria Thiobacillus ferrooxidans, referenced in GRE (2017), can oxidize either sulfide or ferrous iron, and may be involved in either the initial oxidation of pyrite or of the ferrous iron generated form the dissolution of pyrite.

generated at some distance from the location of the pyrite oxidation. For example, acidity in the form of ferrous iron generated by pyrite oxidation in the BRSF can be carried downstream to the equalization pond in the passive treatment system (PTS) for the Site contact water. Knowing how much ferrous iron will be entering the pond is important for estimating how much acid will be generated and need to be neutralized. In addition, the ferrous iron oxidation generates solids (ferric hydroxide, jarosite, and schwertmannite), which can coat the conveyance structures (as "yellow boy") and clog filters. A major risk for implementing PTS during operations is not knowing in advance the ferrous iron load in the water entering the system.

2.1.1.2.3.3.2 "Ferric Iron Oxidation"

GRE (2017) uses the term *"ferric iron oxidation"* for Reaction 4 in Stumm and Morgan (1981), in which pyrite is oxidized by ferric iron, and posits that the humidity cell (HC) test results for sample ARD-74C exhibit the effects of Reaction 4, as stated below (page 24):

> ARD-74C is the most useful sample in the sample dataset. For the first 12 weeks of the test, the cell oxidizes under oxygenated conditions using Equation 1.

> After 12 weeks, ferric iron oxidation begins and the rinsate has reduced pH, increased sulfate concentrations, and increased iron concentrations. This sample demonstrates that Amulsar ARD, even under ideal conditions, has resistance to ARD. As a result, this sample was utilized in subsequent geochemical modeling to define reaction kinetics (GRE, 2014d).

The HC results for sample ARD-74C show a dramatic increase in ARD generation after 12 weeks, with the iron concentration increasing by an order of magnitude and pH decreasing by 0.5 units to less than 3. The GRE (2017) interpretation does not provide an explanation for the source of ferric iron to oxidize the pyrite. Furthermore, the HC ARD-74C behavior is not simply the result of ferric iron oxidation of pyrite. At week 12, the iron concentration is around 5 mg/L, or approximately 0.1 mM. If the iron is ferric iron and reacts with pyrite according to Reaction 4, 0.007 mM of pyrite (1 mole pyrite/14 moles Fe^{3+} x 0.1 mM) will be oxidized, and the iron concentration will increase from 0.10 mM to 0.107 mM ferrous iron. Instead, the iron concentration increases to around 55 mg/L, or approximately 1.0 mM. This significant increase in iron concentration would require a bacterial population to oxidize ferrous iron to ferric iron and a low pH to keep the ferric iron in solution. The rate of pyrite oxidization would be dependent on sufficient populations of the right bacteria. There is no *"resistance to ARD"*. The predominance of one reaction over another reaction cannot be determined from the final concentrations of iron and sulfate or the final pH.

If ferric iron from Reaction 2 is precipitated as ferric hydroxide in Reaction 3, rather than oxidizing pyrite, then the sulfate to iron ratio increases because the dissolved iron concentration decreases. A plot of the concentrations of iron and sulfate for HC 74-C and 76-C (Figure 2.1.1 below) shows that the iron concentrations are slightly below the expected 2:1 line (Reaction 1 or 4) at low concentrations and significantly below the line at the high concentrations.

(Source: GRE, 2014d)
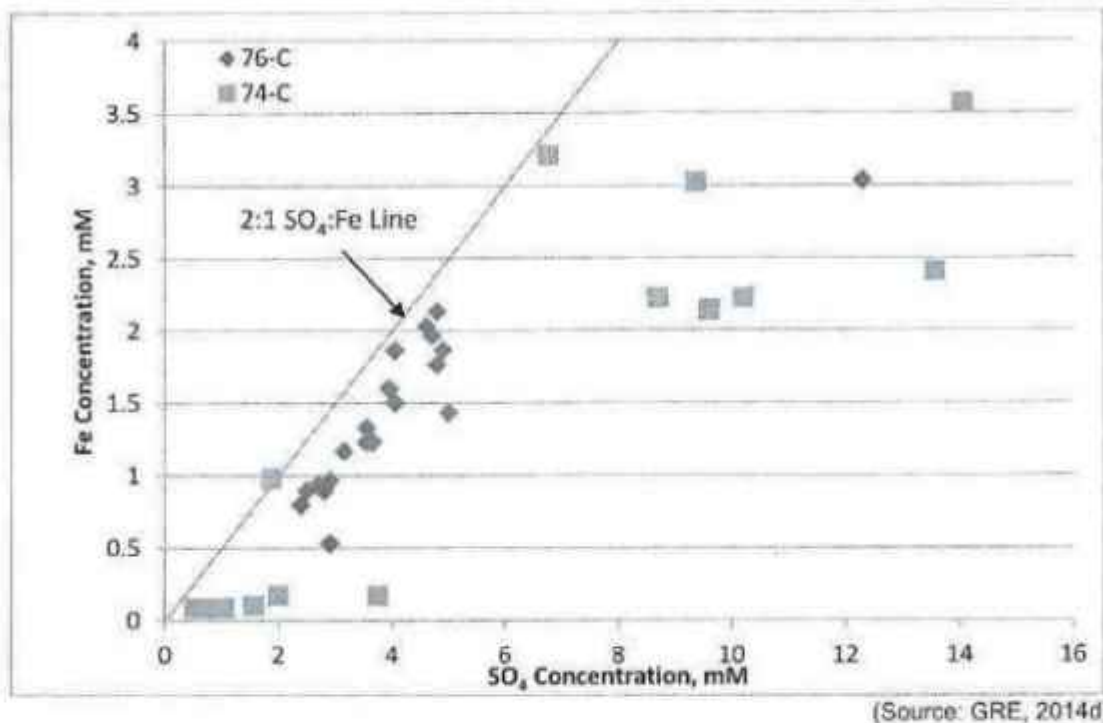
Figure 2.1.1: Comparison of sulfate and iron concentrations for Humidity Cells 74-C and 76-C

Figure 2.1.1 suggests the sample ARD-74C leaching patterns for sulfate and iron reflect the characteristic initially slow pyrite oxidation, with some of the iron precipitating as hydrous ferric oxide. This behavior is particularly evident from the HC leachate analyses at the higher sulfate concentrations (large sulfate/iron ratios).

GRE (2017, page 26) further posits that there is some "*suppression agent*" that is inhibiting the reaction between ferric iron and pyrite, as stated below:

> As a result, the material shows that the LV rock has some natural suppression agent that prevents the formation of ferric iron oxidation. The suppression could be any or all of the below:
>
> - Thiobacillius Ferroxoidants [*sic*][8] have a much slower sulfide reaction rate in cold climates (Sartz, 2011);
> - The argillic texture (with approximately 10% clay content) inhibits the flow of oxygen within the pile, and therefore, oxidation; and/or
> - The LV mineral has some residual natural resistance to ferric iron oxidation that is only overcome in the extraordinary conditions of a long-term humidity cell test.
>
> This natural resistance is a critical conclusion of the characterization of Amulsar mine waste.

The GRE (2017) assessment is misleading. The rate of pyrite oxidation is limited when the bacterial population is low and the pH is too high for ferric iron to be to be soluble.

---

[8] *Thiobacillus ferrooxidans.*

2.1.1.2.3.3.3   Summary of ARD Geochemistry Assessment

GRE (2017) assessment of ARD reactions that would occur in the Amulsar rocks is misleading because the analysis:

1. Fails to recognize the importance of ferrous iron oxidation in the ARD reaction sequence in generating acid and precipitating mineral phases (solids).

2. Postulates that the reaction of pyrite by ferric iron has a higher stoichiometric ratio between pyrite and acidity. The overall reaction between pyrite and ferric iron is the same as the reaction between pyrite and oxygen. The reaction with ferric iron is faster, with the ferric iron acting as a catalyst, but the overall stoichiometry is the same. The ferric iron oxidation is just one of the two pathways for pyrite to be oxidized, and the two pathways cannot be distinguished based on the products generated.

3. Postulates that there is some "*natural suppression agent*" inhibiting the oxidation of pyrite by ferric iron in the LV ores, but the rate of pyrite oxidation is limited when the bacterial population is low and the pH is too high for ferric iron to be to be soluble.

4. Underestimates the potential for ARD generation and the associated water quality, environmental impacts, and water treatment requirements.

The importance of the above assessment of ARD generation on the input water quality to the proposed PTS from the BRSF is discussed in Section 2.1.5.

2.1.1.3 Seismic Hazard Potential

2.1.1.3.1 Tectonic Setting

Section 4.6.1 of the ESIA conveys the tectonic setting. The Project Area is located in the Lesser Caucasus Mountains, which resulted from subduction and closure of the Neo-Tethyan Ocean (Adamia *et al.*, 2011; Grosjean *et al.*, 2018). The northeastern shore of Lake Sevan is adjacent to the suture zone (Figure 4.6.1) and outcrops of the Sevan-Akera ophiolites (Adamia et al., 2011).

2.1.1.3.2 Seismicity

Section 4.6.1 of the ESIA states that the Project Area is NOT located within the major zones of tectonic activity in Armenia, but that the area is geologically active based on the occurrence of young basalt scoria cones. On the other hand, Section 4.6.4 of the ESIA states that "*the Project licence is located within a seismically active region of the Arabia-Eurasia plate boundary zone*" and "*that there are 17 fault zones with a total of 53 fault segments within approximately 250 km of the project site*". Adamia *et al.* (2011) state that the recent geodynamics of the Caucasus and adjacent territories are determined by their position between the still converging Eurasian and Africa-Arabian plates. Furthermore, according to geodetic data, the rate of the convergence is approximately 20-30 mm/yr, of which about 2/3 is likely to be accommodated south of the Lesser Caucasus (Sevan-Akera) ophiolitic suture, mainly in south Armenia, Nakhchevan, northwest Iran, and Eastern Turkey.

Section 4.6.4 of the ESIA indicates that historical records document the occurrence of 107 strongly-felt earthquakes in the Republic of Armenia (RA) from 600 B.C. to 2003. Armenian

records indicate that the Site has experienced strong to very strong shaking at least three times in the last 900 years (Golder, 2013). Figure 4.6.8 (Section 4.6.4 of the ESIA) shows that the Project Area is surrounded by the epicenters of the historic earthquakes and "fault seismic sources".

Two large, devastating earthquakes occurred in the Caucasus in the last 20 to 25 years (Adamia *et al.*, 2011). The first one was the magnitude 6.9 Spitak Earthquake on December 7, 1988, whose epicenter was located within the Lesser Caucasus-Northern Armenia near the Georgian border. The epicenter of the Spitak earthquake was related to the regional Pambak-Sevan fault, constituting a branch of the Sevan-Akera ophiolite suture. Another large seismic event was the magnitude 7.2 Racha earthquake on April 29, 1991. This earthquake was located in Central Georgia in the southern foothills of the Great Caucasus.

Section 4.6.4 of the ESIA indicates that the Pambak-Sevan-Sunik Fault Segment 4 (PSSF4) is located approximately 10 km north of the Project Area (Figure 4.6.8), and that it has an average horizontal slip rate of 1.55 mm/yr (Golder, 2013). Golder's research indicates that the estimated maximum magnitude earthquake from the PSSF4 would be M 7.2 (M is the moment magnitude scale, which is the equivalent of the Richter Magnitude Scale). Golder (2013) states that the PSSF4 is not known to have generated a major earthquake in historic time (approximately the last 10,000 years).

Figure 4.6.8 shows two other active or potentially active faults within 15 to 20 km of the Project Area (PSSF5a and GF5). The estimated maximum magnitude earthquake for the Pambak-Sevan-Sunik Fault Segment 5a (PSSF5a) is M 6.9, with an average horizontal slip rate of 1.3 mm/yr. Golder (2013) assigned an estimated maximum magnitude earthquake of M 7.1 to the Garni Fault Segment 5 (GF5) and an average horizontal slip rate of 1-2 mm/yr. Noteworthy on Figure 2 of Golder (2013) is the location of a 5.0 – 5.9 epicenter 25 - 30 km of the Project Area.

The foregoing text underscores the seismic hazard risk for the Project Area. The historical record of pre-instrumental and instrumental earthquakes indicates that strong to very strong earthquake shaking has probably occurred at the Project Area at least three times in the last 900 years (Golder, 2013). Golder's seismo-tectonic model defines the active and potentially active seismic sources that can contribute to earthquake ground motions in the Project Area. The PSSF4 makes a strong contribution to Project Area seismic hazard because the PSSF fault system is the longest active structure in the RA with the greatest slip rates and strongest earthquakes (Golder, 2013).

Golder's assessment of seismic hazards is generally thorough (see below for further assessment) and conservative. Key mining infrastructure sites that require earthquake ground shaking estimates and seismic design parameters are the HLF, BRSF, open pits, crushing plant, and overland conveyor system. However, it is noteworthy that the recommended seismic parameters are based on ASCE 7-05. The ASCE 7 standard *Minimum Design Loads for Buildings and Other Structures* is the document that the *International Building Code* (IBC) relies on for its structural provisions (Ghosh, 2014). ASCE 7-05 has been replaced by ASCE 7-10 in the 2012 IBC. Major revisions in the ASCE 7 standard include seismic design provision.

2.1.1.3.3 Assessment of Active Faults in the Project Area

Section 4.6.4 of the ESIA states that Golder's field investigations and review of available literature and satellite imagery found no geomorphic evidence for traces of faults or other

tectonic geomorphology within the Project Area, including the proposed sites of the BRSF, HLF, crushing plant, and open pits, and that there is a very low potential for surface fault rupture within the Project Area.

Section 2.1.1.2.2.2.1 of this report makes it clear that there are major faults within the Project Area, including the vicinity of the mine pits and beneath the BRSF. The bounding rivers are expressions of major faults, including potentially the Vorotan River, which may reflect the occurrence of PSSF5a adjacent to the Project Area (Golder, 2013 Figure 2). The PSSF fault system is active. Assuming the southeast course of the reach of the Vorotan River adjacent to much of the Project Area is an expression of PSSF5a, several sharp bends in the Vorotan River southeast of the Project Area are strikingly similar in their northeast orientation (Appendix A), which is consistent with antithetic strike-slip faults associated with dextral displacement of PSSF5a. It is also reasonable to consider that seismicity associated with PSSF5a could result in movement along the other major faults in the Project area, including the Zirak Fault under the BRSF and the Agarakadzor Fault passing through the pit areas.

Only a small, insufficient portion of the satellite image that was provided could be viewed. However, based on the trace of the Agarakadzor Fault on the Geological Map of Vayots Dzor, alternate interpretations of its trajectory or fault splays northeast from the Darb River are indicated on a topographic map and a physiographic map showing the Agarakadzor Fault (Appendix A). The alternate interpretations suggest that the fault and/or the splays pass beneath or near the BRSF. Two notable features on both maps are the large northeast bend in the Vorotan River and the gorge with a tributary of the Darb River. These lineations may be expressions of the fault.

2.1.1.4 Groundwater Flow

Baseline groundwater is summarized in Section 4.8 of the ESIA. The Groundwater Study Area (GSA) was defined as the area within the hydraulic boundaries formed primarily by the Arpa, Darb, and Vorotan Rivers (EISA Section 6.9, Figure 6.9.1[9]). The perimeter of the GSA passes through Kechut Reservoir in the northwest and Spandaryan Reservoir in the southeast. The GSA is appropriately defined. The structural control of the boundary-rivers ensures that flow and transport from the GSA do not traverse these boundaries.

The villages of Kechut, Gndevaz, Saravan, Saralanj, Gorayk, and Ughedzor are located within or immediately adjacent to the GSA. Jermuk is located to the north along the Arpa River, outside this hydraulically-defined GSA. The Jermuk Geothermal Park is north of the Arpa River.

Areas of focused hydrogeological and geotechnical investigations include the sites and vicinities of the proposed mine facilities (the open pit areas, BRSF, and HLF). An area northeast of the HLF and an area southeast of Amulsar Mountain on the east bank of the Vorotan River were also investigated at multiple locations.

2.1.1.4.1 Hydrostratigraphy

Five hydrogeologic units were delineated in the GSA: Colluvium, silicified Upper Volcanics (VC), argillically-altered Lower Volcanic Andesite (LVA), unaltered Lower Volcanics (LV), and Cenozoic Basalt Flows. Brief descriptions are provided:

---

[9] For clarity, Figure 6.9.1 should have been included in Section 4.8 of the ESIA.

Colluvium

Colluvium overlies bedrock throughout much of the GSA, with thickness ranging from less than 1 m up to 20 m. The characteristics of the colluvium are variable. Descriptions range from cobbles with some silt and clay to silty clay with little gravel or cobbles. Permeability is variable. The colluvium is locally saturated in the GSA. In the drainages at lower elevations, silty clay colluvium restricts downward migration of groundwater, generating perched conditions (e.g., in the drainage northeast of the HLF). Fine-grained colluvium locally restricts discharge of groundwater (e.g., in the drainage east of the BRSF), where monitoring wells have water levels above ground surface.

Upper Volcanics (VC)

The silicified VC crop out along the Amulsar Mountain ridge and on its eastern flank and extend to a depth of over 300 m below Amulsar Mountain, with interleaved panels of LVA. Faults and low permeability stratiform panels of LVA compartmentalize perched and seasonal groundwater in the VC. Continuously saturated VC occurs at deeper levels. Permeability is fracture controlled.

Argillically-Altered Lower Volcanic Andesite (LVA)

The argillically-altered LVA occurs within the VC as stratiform interleaved panels and beneath the VC. LVA crops out on the west side and north end of the Amulsar Mountain ridge. The depth of the argillic alteration is unknown. The lateral extent of the halo of argillic (and phyllic) alteration limits the lower elevation of the outcrop to approximately 2,000 m above sea level (asl), where the underlying unaltered LV are exposed at ground surface.

The LVA is described as predominantly amorphous clay in the central area of the ridge. Where LVA is interleaved with VC, the LVA is believed to generate perched groundwater conditions.

Unaltered Lower Volcanics (LV)

The unaltered LV comprise a thick, sub-horizontal sequence of bedded andesite, mass flow breccias, volcanogenic conglomerate, and sedimentary rocks. These rocks crop out all around Amulsar Mountain, extending from approximately 2,000 m asl on the west side of the ridge to the gorge of the Arpa River. The LV is heterogeneous and has variable hydraulic properties, especially at the lower elevations. The andesites within the sequence have low to moderate permeability. The mass flow breccias and volcanogenic conglomerates at the base of the sequence may be highly permeable. The sedimentary rocks are typically clay-rich and have low permeability. Springs issuing from the LV are consistent with high anisotropy in hydraulic conductivity due to the interbedded nature of the sequence.

Cenozoic Basalt Flows

The Cenozoic Basalt Flows overlie the LV and intrusive rocks on plains to the east, west, and south of Amulsar Mountain, and extend northwest from the scoria cone north of the BRSF. The basalts are at least 120 m thick. Locally, the basalts are intensely fractured and permeable. Drilling encountered highly fractured zones within the basalt sequence (possibly flow tops or bottoms or scoria zones) which are interpreted to be transmissive preferential pathways.

2.1.1.4.2 Hydraulic Conductivity

Slug and packer tests were performed in areas that include the ore bodies, the HLF, and the BRSF. These data are summarized in Table 4.8.1 and Appendix 4.8.1 of the ESIA, the latter showing 58 entries of singular test values or ranges, 23 in basalt, 27 in LV, 6 in VC and 2 in colluvium. Many of these entries are for the same location. A map showing the locations of the tests across the GSA is not included in the ESIA or appendices. Therefore, the locations were circled on a map to evaluate the spatial distribution of data (Appendix B).

The number of test locations is 35 (one well in the pit area is not posted). The test locations are concentrated in the pit areas, the BRSF, and the HLF, with 4 tests in an area northeast of the HLF. The 3 tests on the east side of the Vorotan River are outside the GSA and the groundwater model domain.

No pumping tests were undertaken, which is a serious omission in the characterization of hydraulic properties. Pumping tests are a standard procedure for hydraulic characterization and are indispensable for fractured rock. Slug and packer tests provide very localized and discrete data on the hydraulic conductivity. Only long duration pumping tests can provide a good indication of the bulk hydraulic conductivity of fractured rock, which is dependent on the extent of fracturing and fracture connectivity, including bedding-plane structures. Pumping tests should have been performed in the areas of the mine facilities and pits at various depths, as well as several in each rock type across the GSA. If cross-sections had been constructed across the GSA, they may have revealed the occurrence of structures, which would be important in the planning for pumping tests. In addition to the bulk hydraulic properties, pumping tests are essential to identify and assess anisotropy and boundaries (e.g., faults and rivers/streams). Properly planned observation well locations can reveal the locations of boundaries and the extent of influence. For example, the extent of fracture connectivity to a river could be investigated.

Given the environmentally-sensitive setting, the limited distribution of hydraulic tests and the lack of pumping tests are inadequate for characterizing the hydraulic properties across the GSA. Fractured rock has heterogeneous hydraulic properties (Table 4.8.1 and Figure 4.8.8 show a range of 4 or more orders of magnitude), which are dependent on rock type and stratification (which are variable across the GSA) and proximity to structures. The rivers are structurally-controlled, and these structures may be assumed to have uniquely imparted structural fabric and fracture characteristics in their region of influence. Large areas of the GSA, from the mine pits and facilities to the rivers and reservoirs are uncharacterized and cannot be assumed to have the same hydraulic properties of the tested areas.

The water balance for the GSA, estimates of solute transport velocities, and assessment of potential impacts are dependent on good hydraulic characterization. These important objectives of the characterization work can only be attained with a well-constrained numerical groundwater model, especially for this type of geologic setting. The calculated geometric means of [local] hydraulic conductivity (Table 4.8.1 of the ESIA) and the summary of [local] hydraulic conductivity values for impact assessment (Table 4.8.2 of the ESIA) are meaningless for comparisons of rock types, unrepresentative due to the large ranges, and especially unreliable for assessments.

Amulsar Gold Mine - Independent 3rd Party Assessment
Impacts on Water Resources, Geology, Biodiversity and Air Quality

July 22, 2019
31

2.1.1.4.3 Potentiometry

Figure 4.8.13 of the ESIA is a map of contoured mean water levels across the GSA. Figure 4.8.14 in the ESIA is a contour map of water levels measured for a specific period between May 15 and June 15, 2014. Elevations of perennial springs were also used to constrain the contours.

These maps of potentiometry are similar, as expected. The shape of the flow field is broadly consistent with the control of the three major river valleys on groundwater flow and discharge. There are many tributary streams throughout the GSA, and presumably some of these streams are perennial, at least in the lower reaches. The text (Section 4.8 of the ESIA) states that it is likely that groundwater discharges to other major stream valleys to the south of the HLF and to the south of Amulsar Mountain ridge. Elsewhere, the text states that groundwater discharge occurs to streams in the BRSF area, the HLF area, and the valley east of the BRSF, and that it is unlikely these streams are isolated cases. The text further states that groundwater discharge is also likely to occur to similar streams across the GSA and to streams on the lower portions of the eastern face of Amulsar Mountain which have not been monitored or investigated.

As part of the baseline studies, all streams within the GSA should have been characterized as ephemeral or perennial, with corresponding flow rates. The contours of potentiometry should conform to groundwater discharge to all perennial streams, and groundwater flow modeling should incorporate these controls. Figure 4.8.14 of the ESIA shows a potentiometric high west of the Tigranes-Artavasdes ridge area that is inconsistent with topography and ESIA Figure 4.8.13.

These maps of potentiometry are composites of all water levels, irrespective of the depth of the well screens. Noteworthy is that downward vertical gradients are significant in this geologic setting and especially strong at the higher elevations of the ridge area. Heads measured in deep well screens can be much lower than heads in shallow wells. Section 4.8.5 of the ESIA states that all locations surrounding the Amulsar mountain ridge have strong downward vertical components of hydraulic gradient. Even at much lower elevations of the mountain, large head differences are observed between shallow and deep wells in the same location (e.g., Table 4.8.10 of the ESIA). Therefore, the potentiometric maps are very general with respect to true potentiometry. Nevertheless, the general directions of lateral flow implicit in the potentiometric maps are correct.

2.1.1.4.4 Perched Groundwater

Perched groundwater is a recurrent theme in ESIA descriptions of the characterization of groundwater. Although transient perched groundwater occurs, it is less common than assumed. Transient interflow of precipitation and snowmelt could be a perched condition. However, cited examples of large head differences in shallow and deep wells are not evidence for perched groundwater. In this regard, water levels in shallow wells of the pit areas are not all necessarily indicative of perched water. Strong vertical gradients can give the appearance of perched water. Depth-separated water inflows during drilling are also not evidence of perched groundwater. The extent and connectivity of fractures intersecting the borehole account for differences in inflow in an otherwise continuously fracture-saturated section of rock.

2.1.1.4.5 Fracture Flow

Widespread fracture permeability, including bedding-plane fractures, is an important factor in groundwater flow and rates of transport throughout the GSA. The significance of this

phenomenon cannot be understated. Transport of contaminated groundwater is many orders of magnitude greater in fractured media over porous media. The extent of connectivity of fractures, however, determines whether rapid flow and transport occur. Only through conducting pumping tests and groundwater tracer tests can fracture connectivity be assessed.

2.1.1.4.6 Springs

Section 4.8.5 of the ESIA indicates that comprehensive surveys of springs were conducted in November 2013 and May 2014. Included in the surveys are the Jermuk geothermal springs outside the GSA. Drawing 4.8.3 in Appendix 4.8.7 of the ESIA shows the locations of springs in the GSA. The springs were classified as Types 1, 2 and 3:

- **Type 1:** Perennial (continuous flow) geothermal springs representing groundwater discharge associated with regional-scale flow paths. Snowmelt does not influence the flow rate. These springs are located in and around Jermuk.

- **Type 2:** Perennial springs representing groundwater discharge with short- to intermediate-length flow paths. These springs are located on the flanks of Amulsar Mountain ridge and at lower elevations near the Vorotan, Arpa, and Darb Rivers. The flow rates of these springs are seasonally variable. Some of the Type 2 springs with the largest flow rates occur in the BRSF site and the adjacent valley at the north end of the Amulsar Mountain ridge and near Kechut Reservoir at the base of the Cenozoic Basalt.

- **Type 3:** Ephemeral springs (discontinuous flow) characterized by groundwater discharge associated with short flow paths, short-term flow, rapid flow velocities, and generally snowmelt. Many of these springs are located at high elevations on Amulsar Mountain. At lower elevations, the springs represent discharge of interflow from colluvial deposits and shallow weathered rock horizons.

The Type 1 springs around Jermuk are all north of the GSA and would not be impacted by the Mine. Type 2 springs include the Sevan group, which supplies the community of Gndevaz, but is well outside the GSA and would not be impacted by the Mine. Type 3 springs presumably have extremely variable flow rates, dependent on annual precipitation and snowpack, and flow measurements are unnecessary.

Type 2 springs in the northern part of the GSA include the Madikenc group, which supplies the community of Kechut. Table 4.8.11 of the ESIA shows November 2013 flow measurements for only 3 (SP80, SP 83, and SP89) of the 6 springs shown on Drawing 4.8.3 in the vicinity of Kechut. It is unclear whether all 6 springs are part of the Madikenc group. Figure 2 of Appendix 4.9.5 of the ESIA shows several other springs within the GSA in the vicinity of Kechut that apparently weren't evaluated during the survey (no assigned number). The text in Section 4.8.6 of the ESIA states that the November 2013 survey identified only a small number of flowing springs and that a further five flowing locations had no flow estimate. The latter springs are not specified. It is unclear whether the other 3 springs on Drawing 4.8.3 were flowing, as well as the other springs on Figure 2 of Appendix 4.9.5. Because springs in this area supply Kechut, this information should have been provided, and if the springs were flowing, the rates should have been measured.

Type 2 springs in the southern part of the GSA include numerous discharge locations in the vicinity of Benik Pond. The springs and pond are used by the itinerant population of Ughezdor.

The CheyratiDuz springs and the Shlak springs, which supply water for residents of Ughedzor and Saralanj, respectively, are on the south side of the Darb River, outside of the GSA, and would presumably not be impacted by the Project (unclear from available data whether the upper reaches of the Darb River above Ughezdor are perennial, a prerequisite for a groundwater boundary). The potential for impacts to the Pluskandyal springs are even less certain. The Pluskandyal springs are on the east side of the upper reach of the Darb river that flows to the north. Although these springs are also south of the defined GSA, the GSA is not bounded by a river for at least 1,000 m in the area of Vorotan Pass, and it is unclear whether the upper reaches of the Darb River and the other stream on the east side of Vorotan Pass (Porsughlu River?) flowing into Spandaryan Reservoir are perennial.

Flow was not measured at the Pluskandyal springs or the other community springs southeast of Ughezdor. Flow was also not measured at the springs around Benik Pond. The flow rates should have been measured because the springs are water supply for the local communities. Likewise, flow rates for the two springs on the south side of the Porsughlu River that supply water to Gorayk should have been measured.

Section 4.8.6 of the ESIA states that several potentially significant springs were not visited during the November 2013 survey. There were only two surveys, and the November 2013 survey is the only survey in the dry season when perennial springs are identified and characterized. Drawing 4.8.3 in Appendix 4.8.7 shows a large number of springs, especially in the vicinity of the Amulsar Mountain ridge. In general, given the importance of springs to the local communities, including shepherds and ranchers, and the potential for impacts to the springs from the mine pits, the springs flow characterization is inadequate.

2.1.1.4.7 Kechut-Spandaryan Tunnel and Mineral Exploration Adit

Two excavations in the GSA are below depths to groundwater. The most significant excavation/ structure is the Kechut-Spandaryan tunnel, which is a concrete-lined structure traversing the GSA for 21 km from the Spandaryan Reservoir at the southeast extent of the GSA to the Kechut Reservoir at the northwest boundary of the GSA. The tunnel elevations at the Spandaryan Reservoir and Kechut Reservoir, respectively, are approximately 2,033 m asl and 1,998 m asl. The gate at the Spandaryan Reservoir is currently closed. Discharge at the Kechut Reservoir indicates that groundwater is entering the tunnel.

An excavation for mineral exploration (AWO30 adit) east of the BRSF extends from monitoring location AW030 (or SP13.7) with multiple branches at least 650 m to a location below the BRSF valley, where it is estimated to be 80 m below ground surface. A continuous groundwater discharge occurs from the adit.

2.1.1.4.8 Groundwater Recharge Estimate

Section 4.8.6 of the ESIA describes several approaches used to estimate recharge to groundwater. The approaches include baseflow estimates based on the increase in river flow between two spot flow measurement stations on the Vorotan and Darb Rivers during low flow periods combined with estimates of the contributing area of the watershed between the two stations. This approach indicates distributed recharge rates between 290 and 460 mm/year.

The watershed yield approach was used to estimate recharge based on continuous flow data for several stations on the major rivers and tributaries during the periods of November 2012 – May 2013 and December 2013 – May 2014. Average flows were calculated at each station for each

period, unit discharges based on watershed area were determined, and unit discharges were estimated for each month based on the average unit discharges. There is no explanation given in Section 4.8.6 or Section 4.9.5 of the ESIA of how the monthly unit discharges were calculated (Tables 4.9.7 and 4.9.8 of Section 4.9.5 of the ESIA). The calculated monthly unit discharges for December, January, and February of each year were used to calculate the average monthly winter discharges for each year, which were converted to annual discharge or annual equivalent recharge. These recharge values vary widely, from 90 mm/year to 610 mm/year (Table 4.8.13).

Section 4.8.6 of the ESIA concludes that the overall calculated recharge rates from the watershed yield approach are typically between 150 mm/year and 300 mm/year. There is no basis for this statement about typical recharge rates. The average value of the recharge rates in Table 4.8.13 is 254 mm/year.

A water balance methodology (soil moisture balance) was also used to estimate recharge rates. The results are based on a lot of assumptions, including snowpack equivalent precipitation, an estimated percent sublimated, melt release time percentages, runoff estimates, and assumptions about infiltration into exposed bedrock. These results indicate approximately 100 mm/year on Amulsar Mountain and 50 mm/year in lower areas of the GSA.

The summary of Section 4.8.6 of the ESIA concludes that the soil moisture balance approach underestimates recharge, and that based on observed flows and groundwater hydrographs, recharge is considered to be between 200 mm/year and 250 mm/year across much of the GSA, with the greatest rates of infiltration occurring at the higher elevations. However, a large range in values was calculated from the various approaches. The only certain conclusion is that there is considerable uncertainty in the recharge rate. The rate is extremely variable across the GSA. Noteworthy are the recharge estimates based on flow of the major rivers, which are among the higher values of the estimates, ranging from 244 mm/year to 460 mm/year.

2.1.1.5 Surface Water Hydrology

Baseline surface water hydrology is summarized in Section 4.9 of the ESIA. The area of investigations encompasses the Vorotan River valley, the Arpa River valley, the Kechut Reservoir, and the Spandaryan Reservoir. Focused studies were performed on the watersheds of the Vorotan, Arpa, and Darb Rivers.

2.1.1.5.1 Regional Setting

Figure 4.9.1 of the ESIA shows the location of the Amulsar Project in the context of the two major rivers adjacent to the Project Area and Lake Sevan. Lake Sevan 'and the Kechut Reservoir are linked by a tunnel that directs flow by gravity to Lake Sevan. The Spandaryan-Kechut tunnel connects the Spandaryan Reservoir south of the Project Area with the Kechut Reservoir north of the Project Area, but surface water flow does not occur through this tunnel.

Lake Sevan is protected by Armenian law which permits no activity that may negatively impact the lake and its ecosystem. The BRSF lies within the "immediate impact zone" of Lake Sevan.

2.1.1.5.2 Watersheds

Figure 4.9.2 of the ESIA shows mine facilities with respect to the delineated watersheds of the Arpa, Vorotan, and Darb Rivers. Towns and villages are also indicated on this map. The mine pits and the BRSF are located along the surface water divide between the Vorotan and Darb

watersheds. The BRSF lies wholly within the uppermost area of the Arpa watershed. The HLF, adsorption-desorption recovery (ADR) plant, passive water treatment (PWT) system, and crusher are within the Arpa watershed. Table 4.9.1 of the ESIA summarizes some general characteristics of the watersheds.

The Arpa River flows southwest from Kechut Reservoir, passing within 0.6 km of the nearest mine facility (HLF). In the vicinity of the Project Area, the Vorotan River flows generally southeast to the Spandaryan Reservoir, located approximately 6.3 km southeast of the Tigranes-Artavazdes pit. The Darb River flows westward to its confluence with the Arpa River. The Kechut Reservoir is approximately 4.5 km from the nearest mine infrastructure. The Gndevaz Reservoir, east of Gndevaz village in the Arpa River watershed, provides a source of water for livestock. The Jermuk Hydrothermal Springs are upstream of the Kechut Reservoir. Benik's Pond is a small tarn (1 ha) on the west side of Amulsar Mountain in the Darb watershed that is fed by springs and runoff.

2.1.1.5.3 Flow and Stage Monitoring

Long-term public flow data for the major rivers are limited. Historic data are only available for the Vorotan River.

The long-term flow data for the Vorotan River establish its perennial character in the vicinity of the Project Area. The maximum flow rate occurs in the spring during snowmelt. Baseflow is sustained even during dry years at very low rates.

The Vorotan-Borisovka gauge was located in the current footprint of the Spandaryan Reservoir, where it recorded Vorotan River flow from 1943 to 1987 (45 years). The gauging station was relocated to Gorayk, shown on Figure 4.9.6 of the ESIA. The Vorotan-Gorayk gauge recorded flow from 1987 to 2006.

The data for the Borisovka gauge were scaled (using flow/unit area watershed) to the smaller watershed above the Gorayk gauge to produce a data set spanning the entire period from 1943 to 2006. Percentiles of monthly discharge and monthly precipitation were calculated on an annual water year basis using the data for 1962 to 1987 (no explanation was provided for the limited period) and plotted on Figure 4.9.4 of the ESIA. This graph demonstrates that the highest precipitation rates occur in May and June during snowmelt, augmenting discharge, which attains the maximum rates during this period of the year. Discharge during May and June can be as high as 15 to 20 m^3/sec. Discharge from August through March is typically less than 5 m^3/sec.

The Arpa River is also likely naturally perennial adjacent the Project Area. However, the Arpa River reach downstream of the Kechut Reservoir is a regulated waterway, where discharge is dependent on releases from the reservoir. These data are apparently unavailable. Section 4.9.4 of the EISA suggests the hydropower plant west of Gndevaz may divert water directly from the Kechut Reservoir to the plant during low flow periods, potentially augmenting discharge in the Arpa River downstream of that location. The lack of historic flow data for the Darb River and its smaller watershed make it less certain that the river is perennial throughout the study area.   •

Point flow measurements were made by Lydian for the Arpa, Darb, and Vorotan Rivers and several tributaries within the study area in 2008, 2010 and 2011. Continuous flow monitoring was undertaken for these rivers from November 2012 to May 2013 and December 2013 to May 2014.

Locations of continuous and spot flow measurements are posted on Figure 4.9.5 of the ESIA. Figures 4.9.6 and 4.9.7 of the ESIA show the locations of continuous monitoring on the three main rivers and tributaries, respectively, on delineated watersheds. Table 4.9.4 of the ESIA summarizes the spot flow measurements from 2008 to 2015. Appendix 4.9.2 of the ESIA includes specific dates of the spot flow measurements.

The continuous flow monitoring stations established for the Project on the Arpa, Darb, and Vorotan Rivers are generally adequate. Given the size of the Project footprints in relation to the size of the watersheds, any potential impacts to river flow rates would be insignificant and immeasurable with respect to natural discharge variations. Also, the regulated discharge from the Kechut Reservoir would make any interpretations of impacts questionable.

A few apparent deficiencies in continuous flow monitoring are in the vicinity of Vorotan Pass. A station at the bend on the upper Darb River, where the course changes from northward to northwestward, would determine whether flow is perennial or ephemeral in that location (given the importance to groundwater flow modeling). Likewise, a station on the east side of Vorotan Pass on the upper reach of the (Porsughlu River?) flowing into Spandaryan Reservoir would serve the same purpose. A station should also be added to the stream below Benik's Pond to monitor potential effects of the Tigranes-Artavasdes pit. These locations should be incorporated into the monitoring program.

The methods to estimate flow are acceptable. Section 4.9.5 of the ESIA states that the stage dataset is presented graphically as instantaneous and daily average hydrographs in Appendix 4.9.2 and that the record of estimated flow is presented graphically in this appendix. These graphic representations of the data are missing from Appendix 4.9.2 and could not be examined.

Tables 4.9.7 and 4.9.8 of Section 4.9.5 of the ESIA present continuous flow data statistics for several stations on the major rivers and tributaries during the periods of November 2012 – May 2013 and December 2013 – May 2014. Average flows were calculated at each station for each period, unit discharges based on watershed area were determined, and unit discharges were estimated for each month based on the average unit discharges. There is no explanation given in Section 4.8.6 or Section 4.9.5 of the ESIA of how the monthly unit discharges were calculated.

The ESIA does not provide an explanation for the hiatus in continuous flow monitoring between May 2013 and December 2013. The missing time includes some months with presumably the lowest river discharge. Also, Table 4.9.5 of the ESIA reveals missing data for one or both of the continuous monitoring periods at some stations on the major rivers, with only one period of data collection for the one Vorotan station and neither period for both Darb stations. Of the four stations on the Arpa River, only one station collected data for both periods. Termination of the continuous discharge monitoring after May 2014 is questionable. The groundwater balance for the Site and the assessment of solute fate and transport are dependent on good characterization of baseflow.

The plot for the Vorotan River based on long-term public data (ESIA Figure 4.9.4) provides a good summary of the river behavior throughout the year and variations about the mean. A considerable amount of discharge data was collected for the other rivers. However, there is no synthesis of the data (using the spot and continuous measurements) and corresponding

graphical representation of the flow characteristics and variations throughout the year for the Arpa and Darb Rivers.

2.1.1.5.4 Flood Risk

Flood risk is extremely low. The Mine facility closest to a river spatially and in elevation is the HLF. The HLF is at least 200 m above the Arpa River. The Arpa River is a managed watercourse, with mitigation of flood provided by the Kechut Reservoir. All other mine facilities are much further from and higher above the rivers.

2.1.1.6 Surface Water and Groundwater Composition and Quality

Sections 4.8.7, 4.8.9, and 4.9.6 of the ESIA present results of groundwater and surface water composition, quality, and isotopic characterization for the GSA and Jermuk. The characterization was supplemented recently with additional ion and isotopic data (Golder, 2019). Sampling localities include Amulsar Mountain spring waters, Jermuk geothermal springs, the Spandaryan Reservoir, Spandaryan-Kechut tunnel outfall, the Kechut Reservoir, the Gndevaz Reservoir, adits, groundwater wells across the GSA, and numerous locations on the Arpa, Vorotan, and Darb Rivers and tributaries.

2.1.1.6.1 Major Ion and Isotopic Characteristics

Appendix 4.8.4 of the ESIA and Golder (2019) present the results of major ion characteristics on Piper and Durov plots. The most important feature of these plots is a set of points representing Jermuk samples that is completely distinct from all other sampling locations (ESIA Appendix 4.8.4 Figures 1 and 2; Golder, 2019 Figures 1 and 2). Furthermore, the majority of Jermuk samples have distinctly higher conductivity than GSA samples (ESIA Appendix 4.8.4 Figure 11).

One 2013 Jermuk sample location (DWJ4) has some major ion characteristics (ESIA Appendix 4.8.4 Figure 1) similar to the springs east of the Kechut Reservoir (Madikenc group area SP80, SP83, and SP89), some springs and groundwater samples on the Amulsar ridge (ESIA Appendix 4.8.4 Figures 5 and 9), spring 8A south of Arshak Peak (location unknown), the Byuregh spring (location unknown), and groundwater well sample DDGW002 next to the Vorotan River (Drawing 4.8.2). DWJ4 also has characteristics similar to Kechut Reservoir (ESIA Appendix 4.8.4 Figure 7), the Arpa River upstream of Jermuk (Golder, 2019 Figure 1), and the Gndevaz Reservoir. No isotopic data were acquired for DWJ4, but the similarity of the major ion characteristics to waters in so many other locations (including water outside of the GSA) suggests mixing of the spring water with a significant surface water component (precipitation and/or Arpa River water).

Hydrothermal borehole LZ1 (Golder, 2019 Figure 1; location reported as south of Jermuk and east of Kechut) appears to be on a mixing line between two 2018 Jermuk samples (DWJ6 and DWJ7) and DWJ4 (and samples indicated as similar). However, the more enriched $\delta^{13}C$ of the LZ1 sample relative to Jermuk spring waters, including DWJ6 and DWJ7, indicates the composition of this spring does not result from mixing of waters. Higher gross beta of LZ1 than the Jermuk waters supports this interpretation (gross beta in GSA waters is lower than Jermuk waters).

Jermuk geothermal waters and LZ1 have distinctly more depleted $\delta^{18}O$ and δ^2H than GSA waters, the Arpa River, and reservoir waters (ESIA Appendix 4.8.4 Figure 4.8.27; Golder, 2019 Figure 3). The lower isotopic ratios of the geothermal waters relative to surface waters suggest

the source of the springs is old meteoric water that precipitated at historically lower temperatures (larger fractionation factor) than the Present. Geothermal waters derive from long, deep flow paths. Similar depleted oxygen and deuterium isotopes of Illinois Basin groundwaters, considered to be anomalously low, were interpreted to have an origin as Pleistocene (ice age) meteoric water (Faure, 1986). The distinction in isotopic oxygen and hydrogen ratios of the geothermal waters from GSA springs and groundwaters, including springs discharging east of Kechut Reservoir, is consistent with completely separate sources, flow paths, and time frames.

The Jermuk and other geothermal waters have enriched $\delta^{13}C$, in contrast to Amulsar Mountain springs and groundwater, surface water, and precipitation that are depleted (Golder, 2019 Table 2). Other distinctions of the geothermal waters from the GSA waters are high gross beta and, for most samples, gross alpha, significantly enriched $\delta^{34}S$ (vs. distinctly less enriched surface waters and depleted signatures on Amulsar Mountain), and low and relatively consistent $^{87}Sr/^{86}Sr$ compared to Amulsar Mountain and surface waters. The sulfur and strontium isotopic data support the interpretation of long, deep flow paths that pass through mafic rocks with high/enriched $\delta^{34}S$ and lower strontium isotopic signatures than more differentiated rock types like andesite (Faure, 1986).

The high gross beta and alpha of the geothermal waters and low values for the Amulsar Mountain waters require explanation. The more evolved andesitic rocks on Amulsar Mountain should contain relatively high concentrations of the large ion lithophile elements potassium, uranium, and thorium. However, residence times of groundwater on Amulsar Mountain are extremely short compared to the geothermal waters. Accumulation of these radionuclides through preferential leaching on the long flow paths may account for the radioactivity of the geothermal waters.

Samples of the Spandaryan-Kechut outfall in 2013 (ESIA Appendix 4.8.4 Figures 7 and 8) and 2018 (Golder, 2019 Figures 1 and 2) have similar major ion composition to some Amulsar ridge spring and groundwater samples (e.g., ERW1, ERW4, RCAW399, RCAW403, and RCAW408 [ESIA Appendix 4.8.4 Figures 1, 2, 3, 4, 9, and 10; Golder, 2019 Figures 1 and 2]). However, the isotopic signatures of carbon ($\delta^{13}C$) and sulfur ($\delta^{34}S$) on Amulsar Mountain are considerably depleted relative to the tunnel outfall (Golder, 2019 Table 2). Oxygen and deuterium isotopes of the Spandaryan-Kechut outfall are depleted relative to Amulsar Mountain springs and groundwater (ESIA Appendix 4.8.4 Figure 4.8.27; Golder, 2019 Figure 3). This difference suggests the outfall water is entering the tunnel after a moderately long flow path (aged groundwater that originated at lower temperature). The strontium isotopic ratio ($^{87}Sr/^{86}Sr$) of the outfall is also lower than the Amulsar Mountain data, suggesting significant tunnel ingress is not occurring west of the mountain ridge. Isotopic data are lacking for the basaltic rocks to the north, but the low strontium isotopic signatures and relatively high/enriched $\delta^{34}S$ of the outfall suggest groundwater flow through mafic rocks. The outfall data suggest the relatively high sulfate concentration, the distinctly less depleted $\delta^{13}C$ (relative to Amulsar Mountain), the more depleted $\delta^{18}O$ and $\delta^{2}H$, low $^{87}Sr/^{86}Sr$, and the enriched $\delta^{34}S$ of the outfall are consistent with the majority of the tunnel ingress occurring from the basaltic rocks to the north. This interpretation is consistent with shallower groundwater as the Kechut Reservoir is approached, with greater potential for the tunnel to intersect groundwater.

2.1.1.6.2 Surface Water and Groundwater Quality

Surface water and groundwater quality are summarized in ESIA Sections 4.9.6 and 4.8.9, respectively. Surface water monitoring has been conducted since 2007 by Geoteam and the MNP. Geoteam began groundwater quality sampling of wells and springs in 2010. Surface water quality sampling locations are shown on Figure 4.10.1 in Section 4.9 of the ESIA. Groundwater and springs quality sample locations are shown on Drawing 4.8.2 (Section 4.8 of the ESIA).

Assuming Figure 4.10.1 of the ESIA shows current and future surface water sampling locations, the locations appear to be adequate with the exception of no location on the main tributary of the Darb River downstream of AW006 that drains the area of the mine pits. Branches to that tributary extend toward the Erato and Tigranes-Artavasdes pits. A location on that tributary just before the confluence with the Darb River or just downstream of the tributary on the Darb River would ensure all potential impacts from the mine pits are detectable.

The status of current and future groundwater sampling locations is uncertain due to the inclusion of "historical" in the title of Drawing 4.8.2 of the ESIA. The report does not explain why so few springs around Amulsar Mountain and the BRSF are monitored (compared to locations shown on Drawing 4.8.3 of the ESIA) given the importance to livestock. With respect to springs sampling locations shown on Drawing 4.8.2, which appear to have been chosen based on surface water drainage, flow in fractured rock may not follow the local topography. Given the large number of springs that can be monitored (spring melt and low flow conditions), few additional wells are recommended to monitor groundwater quality. These wells should be located north-northwest of the BRSF, southwest of the Arshak pit, and east of the Tigranes-Artavasdes pit. The additional pit wells should not be installed immediately adjacent to the pits and should be screened sufficiently deep to have saturated rock adjacent the well screens the entire year. The existing wells in the vicinity of the pits should be evaluated to ensure they are monitoring groundwater during the dry season.

Table 4.8.20 and Appendix 4.8.5 of the ESIA include the number of baseline samples of springs and wells by location and constituent. In general, the number of sampling events is extremely low (4 or less, many with 2 or less) for characterizing water quality. When examined by analyte, the majority of locations shown in Appendix 4.8.5 have only one analysis, including locations shown on Drawing 4.8.2. Natural variation and sampling and analytical error generate wide ranges of concentrations. These baseline data are extremely deficient. Meaningful statistics of analytes by location cannot be generated for comparison of future concentrations. Many drinking water locations in Table 4.8.22 of the ESIA were sampled only a few times or less.

For surface water, Appendix 4.9.4 of the ESIA provides a listing of the numbers of baseline samples by specific alphanumeric location and constituent. The numbers vary considerably by location, but many range from as few as 1 to 5, many others less than 10, far from sufficient for meaningful statistical analysis.

A statistically meaningful dataset requires about 30 observations for near-normal distributions (moderate skewness, coefficient = 1). Environmental data generally have more than a moderate amount of skew (skew coefficient > 1), requiring approximately 50 samples for a reliable two-sided 95% confidence interval around the mean (Helsel, 2005).

Amulsar Gold Mine - Independent 3rd Party Assessment
Impacts on Water Resources, Geology, Biodiversity and Air Quality

July 22, 2019
40

2.1.2 Seepage, Runoff, Groundwater Flow & Solute Transport Models

2.1.2.1 Pit Seepage Sub-Models

GRE developed a series of numerical unsaturated flow models for estimating time-transient seepage rates to the saturated zone through the rock underlying the walls and bottoms of the evolving and coalescing Tigranes-Artavasdes-Arshak pit (GRE, 2014a). The description of the modeling is concise and is generally sufficient to assess the technical merits. The models include the stages of backfilling of the Tigranes and Artavasdes pits and subsequent placement of topsoil as a growth medium for evapotranspiration according to the mine development plan. The models also simulate the seasonally-occurring pit lake in the Arshak pit resulting from precipitation, snowmelt, and runoff. The seepage flux was incorporated in the regional groundwater flow model.

The modeling was performed stepwise utilizing Vadose/W and Seep/W, two widely used, commercially-available modeling packages/tools capable of generating defensible results. The tools are physical process-based finite-element programs that, used in combination, account for atmospheric and hydrologic processes, including rigorous unsaturated flow for estimating seepage flux. Significantly, for the high elevations of the pit areas, Vadose/W accounts for the accumulation, sublimation, and melting of snowpack. At the time the modeling was performed, Seep/W did not have the capability to calculate the effects of atmospheric processes.

Vadose/W was used to develop one-dimensional (1D) column models for determining the energy and water balance at the ground surface. The models incorporate the slopes of the ground surface. The results were applied as transient water flux boundary conditions at the ground surface of two-dimensional (2D) cross-section models of the Tigranes-Artavasdes-Arshak pit. The variation in elevation of the surface of the Arshak pit lake is applied as a transient head boundary.

The cross-section Seep/W models are very good renditions of the evolving geometry of the pits and placement of backfill. The finite-element meshes appear adequate. Considering the time involved in the physical evolution of the pit geometry and backfill, the discretization of the development that is represented as stages in the models is deemed appropriate. The incorporation of topsoil is not clear at the scale of the images, but the results of the modeling show the effects on infiltration rates.

The use and manipulation of long-term climate data at the Vorotan Pass weather station to develop average daily climate inputs to the model are appropriate. The properties of the material types are based on assumptions due to limited data on the characteristics of the backfill and cover materials and lack of pumping test data. Except for the pit wall rock, the saturated hydraulic conductivities are reasonable, although they are not derived from site-specific data. The rock comprising the pit walls is naturally fractured and blast altered, but the model hydraulic conductivity of 1×10^{-6} cm/sec is very low and underestimated (essentially impermeable). Furthermore, the use of soil-water drainage curves, relative permeability curves, and thermal properties from the model library based on correlation with grain size distribution data and from data for materials at other sites is questionable. Materials from existing mine dumps at the Site and topsoil should have been tested for a range of parameter values. There are no supporting data or literature for the leaf area index and root depth for grass, which have a large range.

The results of the 1D models are incorrect (GRE, 2014a Table 2). The major issue is the conceptualization and high amount of evaporation from exposed rock and backfill (no soil cover). The high values of evaporation for the backfill result from simulated upward movement of soil moisture by capillary forces, a function of incorrect inputs for soil characteristics. Waste rock derived from blasting or ripping usually consists of a loose pile of material with a range of sizes, from large blocks to cobbles and pebbles. Finer grain sizes will settle through the piles, especially near the tops. Most of the incident precipitation and snowmelt infiltrates rapidly through the voids, with runoff dependent on slope and material characteristics. Water is not held under capillary forces. The uncovered VC backfill balance highlights the problem (Table 2 of GRE, 2014a). With zero runoff simulated, the precipitation/snow can only infiltrate and sublimate. The balance indicates that 450 mm of the 603 mm precipitation (net of sublimation) evaporates (75%), implying that capillary forces and soil evaporation account for the loss, or the melt water somehow ponds on the porous rock pile and evaporates. Incorrect runoff coefficients are suspected for the pit walls. Except for haul roads, where some ponding would occur, runoff from incident precipitation and snowmelt on steep walls should occur rapidly. There is virtually no potential to infiltrate with such low simulated permeability (should be higher to account for natural fractures and effects of blasting). Yet, net of sublimation, 60% to 67% of precipitation and snow melt evaporates on the pit walls. With the impermeability of the pit walls simulated, these results should show that most of the precipitation on the pit walls runs off. Much less evaporation should occur in these simulations. Soil water retention and evaporation are expected, however, for the simulation with the soil cover on the backfill.

Another problem with the Table 2 (GRE, 2014a) results is the water balance. The net infiltration based on the tabulated numbers is incorrect. Particularly large discrepancies are evident for both uncovered backfill scenarios.

With such large errors in the 1D models, the quantitative results of the 2D models are also incorrect. In a relative sense, some results of the 2D modeling appear to be qualitatively reasonable. The shapes of the curves of the time-transient infiltration rates to groundwater from the Tigranes pit are consistent with the mine plan. For example, rates peak at year 8 then decline, coincident with the pit being fully backfilled and topsoil emplacement. However, the results for the Artavasdes pit are unclear with respect to the information presented on mine planning. The cross-sections illustrating stages of pit backfill indicate that Artavasdes backfilling is finished at year 8. Peak infiltration is simulated to occur at year 11, suggesting emplacement of topsoil occurs 3 years after the termination of backfilling.

Results for the Arshak pit are incorrect. The pit will be fully excavated at year 8, at which time a closed depression will exist, and a seasonal pit lake will develop. Also, runoff from Artavazdes pit backfill toward Arshak would not occur until approximately year 8. The simulation results indicate a spike in pit bottom seepage at approximately 3.5 years, followed by a low rate, then increasing to a quasi-steady state rate. Pit wall infiltration is shown to peak at approximately year 8, then decline, which is inconsistent with the mine plan of no backfill. The seasonal differences in infiltration rates are conceptually correct.

The fluxes from the pit seepage modeling are incorrect. Use of these fluxes in the regional groundwater flow model results in incorrect assessments of impacts to groundwater levels and springs. Furthermore, solute transport simulations would severely underestimate potential impacts to groundwater and springs from acid mine drainage.

Due to overestimating evaporation and underestimating the runoff, water and mass fluxes reporting (pumped) to the PTS are underestimated, the amount of makeup water is overestimated, and the timing for requiring the PTS is potentially overextended/delayed. The conceptualizations and estimated evaporation, runoff, and groundwater infiltration fluxes are inconsistent with the updated SWWB presented as Appendix 6.10.1 of the ESIA (Golder, 2018).

2.1.2.2 BRSF Runoff Sub-Model

GRE (2014c) presents numerical modeling conducted to estimate time-transient runoff rates from the BRSF and undisturbed ground surface and generated functions for spring and seep flows with the objective of determining the total quantity of water reporting to the BRSF toe pond. The description of the modeling is sufficient to assess the technical merits.

The modeling was performed utilizing Vadose/W. GRE employed 1D column models to determine the energy and water balance at the ground surface for various slopes and surface materials under typical year, wet year, and dry year conditions using long-term climate data at the Vorotan Pass weather station. The use and manipulation of long-term climate data at the Vorotan Pass weather station to develop average daily climate inputs to the model are appropriate, but the wet and dry year inputs are questionable (See Section 2.1.1.1.3 of this report). A 2D Vadose/W model was used to estimate runoff from the undisturbed ground surface. The evolving BRSF and shrinking surface area of undisturbed ground surface were incorporated in the modeling to estimate the time-transient runoff rates. Noteworthy is the stated preliminary status of the modeling due to limited data on spring and seep flows.

GRE (2014c) states that functions were generated representing flow for perennial and ephemeral springs throughout the year. The perennial spring flows were correctly assessed to be part of the total flow reporting to the BRSF toe pond. However, ephemeral spring flows were assumed to abate after the BRSF expanded across their location. This assumption affects the water balance and is not necessarily correct because the sources of discharge may be beyond the footprint of the BRSF, including mine pit areas. Also, the paucity of data on spring flows does not justify a maximum seasonal flow rate for the ephemeral springs occurring at a different time than the perennial springs.

GRE (2014c) indicates that the mine waste was assumed to consist of a wide range of grain sizes to maximize runoff and, thereby, add a conservative factor to the model. The properties of the material types are based on assumptions due to limited data on the characteristics of the backfill and cover materials. The model assigned saturated hydraulic conductivities (Table 2 of GRE, 2014c) are reasonable, assuming the low value for the argillized LV backfill represents the 0.5 m thick compaction zone that is presumably a design feature at the top of the PAG rock. However, the selection of other model material properties is questionable (See Section 2.1.2.1 of this report). The conservatism for the sake of calculating runoff is not conservative for estimating seepage (See Sections 2.1.2.1 and 2.1.2.3.1 of this report). Also, as noted above, there are no supporting data or literature for the leaf area index and root depth for grass.

Figure 11 (GRE, 2014c) includes runoff results from LV waste rock for a typical year. GRE (2014c) states that very little runoff is generated by the model (an expected result) due to the coarse texture and relatively high permeability of the waste, with the potential for subsequent evaporation of soil moisture. This statement underscores the misconception about the fate of the moisture that infiltrates, which is manifested in the simulations as high soil moisture evaporation and low seepage rates (See Sections 2.1.2.1 and 2.1.2.3.1 of this report). The

evaporation is inconsistent with the coarse texture and high permeability of the exposed waste rock pile.

Due to overestimating evaporation and underestimating the runoff, water and mass fluxes reporting to the PTS are underestimated, the amount of makeup water is overestimated, and the timing for requiring the PTS is potentially overextended/delayed. The conceptualizations and estimated evaporation and runoff fluxes are inconsistent with the updated SWWB (Golder, 2018).

2.1.2.3 BRSF Seepage Sub-Model

2.1.2.3.1 Seepage Through Waste Rock

GRE performed numerical unsaturated flow modeling to estimate time-transient seepage rates through the BRSF during operations and the post-closure period (GRE, 2014b). The description of the BRSF development and the modeling are adequate to assess the technical merits.

The modeling was performed utilizing Vadose/W, described in Section 2.1.2.1 of this report. GRE utilized the results of 1D column models that estimate the amount and timing of infiltration into the materials that will be exposed at the surface of the BRSF at various stages and after closure. These models were previously developed to estimate runoff from the BRSF (GRE, 2014c). The results were incorporated into a series of 2D Vadose/W models as transient water flux boundary conditions at the ground surface. The 2D models represent the evolution of the BRSF along a northeast-trending cross-section that approximately follows the axis of the BRSF valley, where the greatest thickness of waste rock will be deposited.

An example was presented of an infiltration function from the 1D modeling for the upper volcanic rock waste during operations (GRE, 2014b Figure 1). The plotted results show an infiltration peak corresponding to the April-May snowmelt event, followed by summer and early fall negative infiltration (evaporation from the waste rock). The text clarifies that a portion of the moisture near the top of the waste rock is lost to the atmosphere. This evaporation (attaining a rate of about 1460 mm/year), resulting from capillary forces drawing moisture to the surface of the waste rock, is unrealistic and supports the belief that the evaporation from the pit backfill, discussed in Section 2.1.2.1 of this report, results from incorrect inputs for rock pile properties.

A 2D infiltration function (GRE, 2014b Figure 2), representing post-closure conditions with a soil cover, shows no evapotranspiration during the summer months because the function was edited to remove this water loss. The statement in the text that "it is unrealistic to assume so much water could be removed by evaporation" is an awareness that the model is incorrect. The problem caused by the incorrect soil characteristics for the VC waste rock (incorrect conceptualization of a loose rock pile) was compounded by the conceptually correct implementation of capillary forces in the soil cover. Moisture was being supplied to the cover soil from the underlying rock. The alteration of the 2D function to remove evaporation, however, did not correct the model. The lack of elevated infiltration during the spring snow melt (GRE, 2014b Figure 2) is the result of the combined effects of the incorrectly simulated capillary forces in the VC waste rock and the correct implementation of capillary forces in the overlying soil cover.

The calculated volumetric fluxes that report to the base of the BRSF are greatly underestimated due to incorrect model parameterization. The underestimated water fluxes translate to underestimated mass fluxes related to contact of the seepage with the acid-generating rocks. These underestimates negatively impact the calculated net water fluxes and concentrations

resulting from the mixing of ARD with fluxes from the springs and seeps beneath the BRSF. Consequently, water and mass fluxes reporting to the PTS are underestimated, the amount of makeup water is overestimated, and the timing for requiring the PTS is potentially delayed.

2.1.2.3.2 Seepage to Groundwater

GRE (2014g) simulated seepage to groundwater through the BRSF foundation (clay liner) beneath the overdrain (consisting of 5m of VC rock) under the assumption that some of the seepage passing through the waste rock pile will continue migrating vertically rather than flow along the base of the overdrain. Seepage through the BRSF foundation was evaluated for four conditions (GRE, 2014g Figure 2): 1) basalt underlying the clay liner, LVA underlying the clay liner, springs discharging through LVA underlying the clay liner, and the stream carrying spring discharge water on the clay liner underlain by LVA. The seepage was simulated for 1,000 years. The descriptions of the modeling are incomplete.

Simulations of seepage into the LVA and basalt were performed with Vadose/W based on the same material properties of the waste rock and other model parameters that were used to estimate seepage rates through the waste rock pile described in Section 2.1.2.3.1 of this report. The boundary conditions at the base of the models are not provided in the text. A simple Vadose/W model was used to simulate seepage along a profile through the area of the stream channel based on simulated lateral flow through the VC overdrain on the clay liner, with assumptions of head at the upstream and downstream locations of the channel (implemented with constant heads) and a single water level in the underlying argillically-altered LV (implemented with constant head). The area of the BRSF foundation underlain by springs was not modeled due to the interpretation that seepage would be prevented by the upward vertical gradients associated with groundwater discharging at ground surface.

Based on the information provided, it cannot be determined whether the simulated seepage rates into the basalt and the argillically-altered LV are conservative or underestimated. The simulated seepage fluxes reporting to the base of the waste rock pile are underestimated for the same reasons described in Section 2.1.2.3.1 of this report. However, without knowing the boundary conditions at the base of the pile, it cannot be determined if the models are simulating saturated head building on the clay liner without potential for lateral drainage through the VC overdrain (conservative). If boundary conditions provide for lateral drainage, the slope of the compacted clay surface is unknown, but the seepage fluxes to groundwater are likely underestimated due to the underestimated fluxes reporting to the base of the rock pile. Noteworthy are seepage rates through the LVA that are higher than seepage rates through the basalt (GRE, 2014g Table 1). The basalt is considerably more permeable, and both media are overlain by clay. The clay placed over the basalt is modeled with a hydraulic conductivity of 1×10^{-6} cm/sec. The hydraulic conductivity assumed for the compacted clayey soil foundation material in GRE (2014c) is 8.4×10^{-7} cm/sec. The higher seepage rates through the LVA are inconsistent with these values. The simulated seepage rate to groundwater beneath the area of the stream is low, as expected, due to preferential lateral flow through the VC underdrain and slotted pipes.

2.1.2.4 HLF Solute Transport Sub-Model

Golder (2014b) presents an assessment of the potential impacts to groundwater and surface water that could result from leakage through the membrane liners of the heap leach pad (HLP) and pregnant solution pond (PSP) during operations through post-closure. The description of

the design of the HLF, the conceptual model, and the solute transport modeling are adequate to assess the technical merits.

The analyses were performed with the assistance of the GoldSim Contaminant Transport Module. The modeling software is purported to have been used to address complex contaminant transport problems worldwide, especially in radioactive waste management, mining, and water resources. An overview of the modeling tool is provided in the HLF assessment report, which indicates the model utilizes analytical solutions. The use of analytical solutions may be acceptable for simulating local leakage scenarios and approximating local vertical fluxes, particularly with the stochastic algorithms, but the application of the model alone to simulate transport in the complex saturated zone within the GSA is questionable, especially with the existence of a numerical groundwater model (FEFLOW used for modeling groundwater flow and could have been coupled with GoldSim). The numerical groundwater model should incorporate water and contaminant fluxes from all potential sources to produce an integrated assessment of impacts to groundwater and surface water. On this basis alone, the results of the GoldSim transport modeling may be dismissed. However, there are other overarching issues with the modeling, primarily with the assumed source concentrations.

A major flaw in the transport modeling is the absence of the chemical analysis of the pregnant leach solution (PLS). Golder (2014b Section 2.1.2.1) states that the attenuation mechanisms[10] of weak acid dissociable (WAD) cyanide within the heap are complex and are only reliably assessed through laboratory testing of the leach process or in heap operation. Compounding the source term issue is the assumption that the chemical analyses (Golder, 2014b Table 2) of barren leach solutions (BLS) are suitable substitutes for the PLS. That assumption is incorrect due to the processes involved in separating the gold from the PLS. Furthermore, assuming the concentrations of metals in the PLS are up to 2 times the concentrations reported in the BLS is unsatisfactory because the factor differences between the two analyses of BLS are much greater than 2 for many of the constituents.

The heap leach solution (HLS) will be in a closed loop with zero discharge. Volume control is through evaporation. Loading with sodium cyanide, hydrochloric acid, sodium hydroxide, and lime (to crushed ore) occurs continually at various stages. Drainage from the BRSF will also be added to the leach solution for the first 5 years, contributing additional load (e.g., sulfate and metals), and there will be ammonium nitrate residue from blasting. After 10 years, the concentrations of many constituents, including metals, will be higher than shown in Golder (2014b Table 2).

Other issues with the BLS and final detoxified solutions Golder (2014b Table 2) include total alkalinities that are not the sums of the components (bicarbonate, carbonate, and hydroxide). Particularly concerning is the zero bicarbonate in solution 61790. There is also charge balance error in the solutions.

The assumptions for the vertical flow modeling are conservative. However, the absence of results from unsaturated flow modeling of infiltration through the post-closure cover at the time the HLP assessment was performed is unsatisfactory.

---

[10] Volatilization, complexation, and precipitation

Simulated transport species omit chloride, the most conservative/mobile solute in groundwater. Furthermore, selenium should be included in transport simulations due to the detrimental impacts to fish (USEPA, 2016). The significance of these omissions cannot be determined in light of the uncertainty in the overall assessment and in the modeling conceptualizations.

The text is unclear with respect to Scenario 1 shallow impacted groundwater that emerges in the stream bed southwest of the HLF. In one description of the modeling (Golder, 2014b Section 2.3), the constituent mass is not discharged to the Arpa River "as this is considered in Scenario 2". If that is the case, the simulated extended path length through the subsurface to the Arpa River incorrectly provides additional attenuation and delay that would not occur in surface water. In Section 3.4.3 and Section 4.0, for Scenario 1, this discharge is stated to be captured before discharging to the Arpa River. It is unclear what infrastructure is planned for this capture and how or why additional impacted shallow groundwater would not discharge further to the southwest in the stream bed for flow into the Arpa River.

In Section 3.4.3.3 (Golder, 2014b), there is a discussion about monitoring streamflow and quality of the shallow groundwater emerging in the drainage southwest of the HLF during operations. Golder (2014b) states that if leakage is detected and modifications to the HLF operations do not result in water quality improvements, then other industry-standard seepage mitigation measures would be implemented to prevent offsite migration of shallow groundwater. Golder (2014b) does not specify or provide details on the seepage control measures nor does it explain as to how changes in HLF operations can mitigate a design or construction flaw buried beneath the heap. Moreover, the approach to implement unspecified mitigation measures to prevent offsite migration of shallow contaminated groundwater is a reactive rather than proactive approach to protecting the Arpa River.

2.1.2.5 Regional Groundwater Flow Model

Golder constructed a three-dimensional groundwater flow model for the GSA with the intention of improving understanding of the hydrogeologic setting of the proposed mine site and to estimate groundwater inflow to the mine pits (Golder, 2014a). The report describes the model construction, inputs, calibration to baseline conditions, and predictions of impacts to groundwater quantity for operational and post-closure phases of the mine. Particle tracking was used to illustrate simulated groundwater flow pathways. The report was evaluated for the technical merits of the model with respect to the Site hydrology and hydrogeology, its reliability for predictive analysis, as well as the numerical modeling procedures. The evaluation presented in the following text addresses the most significant aspects of the modeling.

Noteworthy is that the model was not used as a tool in the planning phase of locating mine facilities for minimizing risk to the environment (e.g., Myers, 2016). A significant omission of the numerical modeling is the performance of solute transport simulations for predicting impacts to the quality of groundwater and surface water.

The modeling was performed with FEFLOW, a widely used, commercially-available groundwater modeling tool capable of generating defensible results. Finite-element groundwater modeling tools are uniquely suited for incorporating complex geologic structure. FEFLOW can simulate fully-saturated and variably-saturated conditions and contaminant transport. Capabilities for facilitating parameter estimation, highly parameterized inversion, and uncertainty analysis (e.g., Doherty, 2010) are integrated in the commercial modeling package.

The model domain is delineated by groundwater divides of the major rivers along almost the entire perimeter and is appropriate for assessing potential environmental impacts of the mine. Discretization by the numerical mesh is generally appropriate over the majority of the GSA for a model of this scale.

Constant head boundaries were set along the major rivers with head corresponding to the channel bottom to a depth of 100 meters (i.e., all model layers within 100 m depth of the surface were assigned the same head). This approach is incorrect because it simulates perfect hydraulic connection between the rivers and rock to 100 meters depth (i.e., precluding upward hydraulic gradients). It is inconsistent with the conceptual model illustrations showing upward gradients beneath the rivers as expected for groundwater flow paths to gaining rivers in this setting. Flow paths illustrated by results of particle tracking simulations are depressed because the effects of upward vertical gradients that occur near the rivers are artificially eliminated beneath the rivers in the flow simulations (due to this incorrect boundary condition).

Section 4.9.5 of the EISA states that numerous minor perennial tributaries originating on the slopes of Amulsar and the plateau to the east of the Vorotan feed the Darb and Vorotan Rivers. These perennial streams should have been included in the model.

A potentially unnecessarily long no-flow boundary was used along the southern perimeter, forcing flow parallel to this boundary to the northwest and southeast. A boundary condition that permits discharge (seepage face) at appropriate elevations could have been utilized along the upper Darb and the Porsughlu River (assuming both rivers are perennial in those locations) that flows to the southeast toward the Spandaryan Reservoir for nearly the entire length of the simulated no-flow boundary. No-flow would be appropriate for a very short length near the topographic divide. The impact of the long no-flow boundary on simulated flow from Amulsar Peak cannot be determined based on available information.

Seepage faces were used to simulate perennial springs discharges. Appendix 6.9.1 of the ESIA states that the elevations of the perennial springs were not used as groundwater elevation calibration points. The seepage faces must be defined with appropriate elevations. The statement is troubling because it suggests imprecision in setting the elevations to ensure the model simulates springs discharge (i.e., at lower elevations than the springs).

In principle, the hydrogeologic conceptual model is incorporated into the model. However, the model is an extremely generalized representation of the hydrology and hydrogeology of the GSA. The model embodies the principal topographic and hydrologic elements of the conceptual model comprised of Amulsar Mountain surrounded by the Arpa, Vorotan, and Darb Rivers. Discharge is simulated to the rivers and perennial springs. Except for local higher recharge in the BRSF valley and adjacent basins (250 mm/yr), the final calibrated net recharge is uniform at 200 mm/yr. This uniform recharge rate is generally low, with respect to winter (baseflow) measurements of the major rivers (Table 4.8.13 in Section 4.8.6 of the ESIA), from which annual values were calculated, which reportedly underestimate of the annual recharge.

Five conceptual hydrogeologic units were delineated in the GSA: Colluvium, VC, LVA, LV, and Basalt. With the exception of distinguishing a deep section of LV for assigning model properties, each of the five hydrogeologic units is represented by a single set of hydraulic properties, i.e., all six model units are numerically homogenous, in spite of the hydraulic test data showing 4 or more orders of magnitude variation in hydraulic conductivity for each rock type. This deficiency

can have a significant effect on the model predictions (e.g., will not identify preferential flow pathways).

The geology in the pit areas is poorly represented. Faults are completely absent in the model. Geologic modeling of the Amulsar Mountain ridge area (Holcombe, 2013) reveals a level of simplicity defined by a major fault architecture with large displacements (> 250 m) and large-scale slabs or stacked sequences of VC and LVA separated by thrust fault planes that should have been incorporated in the groundwater model. Some LVA panels were correlated through multiple fault blocks. Complex structural blocks could be represented as simple hydraulically distinct units for calibration. The major high-angle normal faults and low-angle thrust faults are likely barriers to groundwater flow, which is supported by the occurrence of abundant clay gouge inferred to have been transported during slip along LVA units. Some faults may be conduits for groundwater flow. Incorporation of these structural and lithologic elements, with calibration to water levels in wells screened in discrete lithologies and discharges of springs, holds the potential to understand many of the major ephemeral springs and better quantify net recharge to the underlying regional groundwater flow system.

The simplistic numerical representation of the subsurface in the existing model is inadequate for making quantitative predictions. Notwithstanding this inadequacy, numerous quantitative predictions, which are unreliable, were made. Transient simulations were performed to estimate pit inflows, but the model is also a poor predictor because a transient calibration was not performed, such as simulation of a pumping test.

The baseline model (calibration) represents average annual conditions as a steady-state simulation. The model was calibrated to the average groundwater elevations recorded in monitoring wells in the GSA[11]. Even with this simplification of site conditions and water level targets, there are many significant calibration errors (differences between simulated and target water levels). Twenty-two of forty-one calibration targets (54%) have errors of 25 meters and more, and fourteen targets (34%) have errors of 40 meters and more, ranging up to 96 meters (twice the maximum recorded seasonal range in water levels). Even without considering recorded seasonal differences in groundwater levels up to 48 meters in wells, the steady-state model, purported to represent average conditions, with such large calibration errors to predict groundwater elevations is unreliable.

Estimated errors in groundwater levels up to 25 m for the purpose of calibration are excessive. The report indicates that well elevations were determined in 40% of the locations with a hand-held GPS and assigned an incremental error of 20 m. These devices are typically accurate within 10 m. The liberal estimated error appears to be a justification of the large model water level errors.

Despite the large model water level errors, the model was used to estimate operational water levels beneath the BRSF area (simulated baseline water level errors up to 80 m), the HLF area (simulated baseline water level errors up to 37 m), and the mine pits (simulated baseline water level errors up to 90 m). Furthermore, the baseline model results were used to delineate the distribution of head at or above ground surface across the GSA which, only locally, roughly corresponds to the locations of springs. With such large errors in calibration water levels, the

---

[11]This procedure is inconsistent with a statement made by Lydian representatives during the March 28, 2019 presentation that model calibration was based on springs' discharges, not groundwater elevations.

model is a poor indicator of head above ground surface and a poor indicator of the effects of mining activities on groundwater levels and groundwater flows (springs, river discharges, pit inflows). Noteworthy are the omissions of springs elevations and discharges as targets in the calibration (inconsistent with statement made during Lydian's March 28, 2019 presentation). Golder (2014a) acknowledges the model's inability to predict pit inflows, yet pit inflows and the impacts of pit dewatering on water levels and on springs discharges and river flows were reported.

Extremely large changes in head are predicted from reduced recharge over the footprints of facilities (up to 69 m beneath the BRSF in the LVA, greater than maximum recorded seasonal changes). These results are indicative of calibrated hydraulic conductivity values that are too low, not reflecting fracture permeability and connectivity. Section 4.8.4 of the ESIA states that hydrographs for wells in the BRSF site indicate that groundwater levels rise rapidly in the Spring in response to snowmelt and decline rapidly following snowmelt. This behavior is indicative of fracture permeability and connectivity. The predicted changes in groundwater levels are unrealistic. Fractures beneath the BRSF are connected with fractures outside the BRSF footprint. Furthermore, model hydraulic conductivity values are directly proportional to model recharge values, and the recharge is low.

Especially conspicuous is the 1×10^{-8} m/s hydraulic conductivity of LVA (Golder, 2014a Table 4), which is essentially impermeable. Considering the extent of structural deformation of the volcanic rocks on Amulsar Mountain, the fracture permeability in the LVA, which will be higher than the matrix permeability, will control the groundwater flow. Argillized tuffaceous rocks at Yucca Mountain, for example, have hydraulic conductivities ranging from approximately 1×10^{-5} to 1×10^{-4} m/s (Gelden, 2004). Table 4.8.1 of the ESIA shows a high end of 3×10^{-5} m/s from tests in LVA. Another conspicuous calibrated hydraulic conductivity value is for the VC (2×10^{-7} m/s), which is lower than unaltered LV (6×10^{-7} m/s). This silicified rock is brittle and highly fractured (average RQD of 0.40; Table 1, App. 6.9.1), especially considering its occurrence in the area of greatest structural deformation, and thus should have a higher hydraulic conductivity than the unaltered LV. Table 4.8.1 of the ESIA shows a high end of 3×10^{-4} m/s from tests in VC. The unaltered LV has a calibrated hydraulic conductivity of 6×10^{-7} m/s. Table 4.8.1 of the ESIA shows a high end of 2×10^{-4} m/s from tests in LV. For fractured rocks, the assumed uniform hydraulic conductivity anisotropy ratio (K_h/K_v) of 100 for the LV is conspicuously high and is contributing to the low calibrated recharge. The basalt, described as intensely fractured (average RQD of 0.19), is missing from Table 4, and cannot be evaluated. The colluvium hydraulic conductivity is reasonable, but it is unclear why wells within the colluvium were not included in the calibration.

An outdated approach (ASTM, 2016) was used to perform model sensitivity analysis. The results were not used or intended to be used to collect additional data for the most sensitive parameters to better constrain the model (Myers, 2016), nor were the results used to guide calibration of the model because the procedure was performed after calibration. The results determined that the model is very sensitive to the hydraulic conductivity of the colluvium, yet water levels in the colluvium were not used in calibration. The problem with this type of sensitivity analysis is that the model is no longer calibrated after making a large change to a single parameter. The modified model cannot be used with any confidence to evaluate uncertainty of predictions.

Given the complexity of the geology of the GSA, the model should be calibrated using highly parameterized inversion (regularization techniques) to generate the expected heterogeneous and variably anisotropic hydraulic conductivity values for each hydrogeologic unit in order to match measured heads and flows. The uncertainty of the results of predictive simulations based on the non-unique solution (all models are non-unique) could then be evaluated. Predictive uncertainty analysis determines the set of possible solutions that similarly meet the calibration objective function (the sum of squares of model errors), and predictive results are generated for each solution as part of risk analysis.

The model is a qualitative or screening tool, at best, for illustrating the generalized configuration of the potentiometric surface, generalized groundwater flow paths, and conceptual responses to mining and associated operational activities on groundwater levels. The model certainly does not contribute to understanding the hydrogeologic setting of the proposed mine. If a quantitative model was the objective for predicting changes in water levels and flows, more hydraulic testing (especially pumping tests) should have been performed, and considerably more effort should have been devoted to incorporating the main structural and stratigraphic elements in the pit areas. Long-term, large-scale pumping tests should have been performed in the areas of the mine facilities and pits at various depths, as well as several in each rock type across the GSA.

Surface water and groundwater are interconnected. Water is exchanged in both directions. There are a host of factors influencing groundwater recharge, which varies significantly in space and time at all scales. Assuming some fixed amount of water percolates through the ground uniformly across large areas of the site and recharges groundwater at a rate that is constant with time is an overly simplistic approach that leads to poor model representation of subsurface properties and unreliable conclusions about surface water and groundwater. Given the scope of the Mine and its potential impacts on the environment, watershed modeling should have been employed. Recharge values are best constrained using an integrated hydrologic modeling approach which links watershed modeling and groundwater modeling.

The report (Golder, 2014a) states that the model indicates the Spandaryan-Kechut tunnel intersects the water table along its length, but with little influence on the water table in the south and center of the model. Noteworthy are the considerably depleted isotopic signatures of carbon ($\delta^{13}C$) and sulfur ($\delta^{34}S$) on Amulsar Mountain relative to the tunnel outfall (Golder, 2019 Table 2). The strontium isotopic ratio ($^{87}Sr/^{88}Sr$) of the outfall is also lower than the Amulsar Mountain data, suggesting significant tunnel ingress is not occurring west of the mountain ridge. Isotopic data are lacking for the basaltic rocks to the north, but mafic rocks typically have lower strontium isotopic signatures than more differentiated types (e.g., andesite) and high/enriched $\delta^{34}S$ (Faure, 1986). The outfall data suggest the relatively high sulfate concentration, the distinctly less depleted $\delta^{13}C$ (relative to Amulsar Mountain), and the enriched $\delta^{34}S$ of the outfall are consistent with the majority of the tunnel ingress occurring from the basaltic rocks to the north.

A notable inconsistency in the report (Golder, 2014a) is apparent in the model calibration section with respect to estimated percentages of the catchments of the rivers within the model domain. In this section, the text states that approximately 20% of the Vorotan River, 60% of the Arpa River, and 45% of the Darb River catchments lie within the model domain. These percentages contrast with 15% for the Vorotan River, 15% for the Arpa River, and 30% for the Darb River stated in Section 4.6. These discrepancies suggest adjustments of the estimates were made to suggest that simulated Vorotan and Arpa discharges are correct.

The model does not correctly represent the GSA water balance. Total recharge is low with respect to estimated river baseflows. Furthermore, the model is intended to represent average annual conditions (calibration to average groundwater levels). The average levels incorporate high late spring and early summer groundwater levels resulting from infiltration of spring snowmelt. Much of this infiltration discharges as ephemeral springs and is not part of baseflow. In order for the model to support these higher average groundwater levels, in combination with the low recharge, low hydraulic conductivity values were required (lower than fractured rock). Less water is moving through the simulated rocks than the actual quantity. Furthermore, the simulated rates of flow and transport (advective velocities in the particle tracking simulations) are too low.

2.1.3 Water Resources Impacts Assessment

Potential impacts to surface waters and groundwater from the BRSF, the HLF, and the mine pits were estimated with the assistance of sub-models and water balance calculations. The sub-models are addressed in Section 2.1.2 of this report. The assessments pertain to springs, rivers, reservoirs, community water supplies, and the Spandaryan-Kechut tunnel. Emphasis is placed on the post-closure period for the analysis of impacts. The impacts assessments are not based on an integrated approach that includes all sources of contaminants. Limited solute transport simulations were made using an analytical model instead of the regional numerical groundwater flow model to simulate the complex system.

2.1.3.1 BRSF

Section 2.1.2.3 of this report discusses the simulated water balance for the BRSF (GRE, 2014b,c). The calculated volumetric fluxes that report to the base of the BRSF are greatly underestimated due to incorrect parameterization of the infiltration model. The underestimated water fluxes translate to underestimated leachate mass fluxes related to contact of the infiltration water with the acid-generating rocks. Based on the information provided by GRE, the potential seepage rates to, and mass loading of, groundwater are also underestimated.

Geochemical modeling was performed to estimate the post-closure water quality that may seep to groundwater beneath the BRSF (GRE, 2014g). The description of this modeling, including treatment of detection limits and the basis for the initial water qualities and oxygen penetration depth, is essentially the same as summarized in Section 2.1.3.3.2 below for seepage through the backfill in the Tigranes-Artavasdes pit. However, the specifics of the HC test solutions and the resulting compositions of the initial solutions (VC and LV) are not included. Otherwise, the same charge balancing procedure was used (with fluoride and sodium) and the same equilibrations under oxic then anoxic conditions were performed. The solutions were mixed after the oxic equilibration. Appendix C of this report (table showing required PHREEQC model details) shows the equilibrated solid phases. In contrast to the cover on the backfill of the Tigranes-Artavasdes pit, the BRSF ARD rock is overlain by 0.2 m of topsoil, 1 m of clay, and 0.5 m VC waste rock.

The text of the report (GRE, 2014g) states that simulated leachate water quality is consistent with samples of long-term ARD reactions that are occurring in unmitigated LV waste piles located in Site 13 and Site 27. The simulated pH of the leachate is 3.0, similar to Site 27 leachate. Most of the simulated concentrations are much greater than the observed concentrations, which is consistent with a much longer vertical flow path than the existing waste piles. The notable exception is iron. The simulated concentration arriving at the base of the

waste pile is only 0.5 mg/L, compared to 3.2 mg/L in the Site 27 leachate (ESIA Appendix 4.6.2 Table/Appendix F-1), which has a similar pH of 3.3. This difference is indicative of inappropriate specification of iron phases in the equilibrium modeling (see discussion of Pit Water Runoff below).

Assessment of impacts to groundwater was not done, i.e., no mixing calculations were performed. Transport was not simulated in the regional groundwater model, nor by any other means.

2.1.3.2 HLF

The assessment of potential impacts from the HLF is discussed in Section 2.1.2.4 of this report. Use of inappropriate source concentrations is the major issue with the solute transport modeling. Also, the assessment does not integrate potential impacts from the BRSF and the mine pits.

2.1.3.3 Mine Pits

The water fluxes (runoff, infiltration through backfill, seepage to groundwater) from the pit seepage modeling of the Tigranes-Artavasdes-Arshak pit are significantly underestimated (Section 2.1.2.1 of this report). Insufficient information is provided in the report for the Erato post-closure pit water balance (Golder, 2014c) to fully assess the pit inflows, the pit lake level and volume, and the calculated seepage rate to groundwater. However, perched water inflows are based on the incorrect, low recharge rate determined by the groundwater model calibration. Noteworthy is that only 40% of precipitation on the pit walls was assumed to report to the pit bottom based on a water balance for the HLF (cited report[12] was unavailable). This assumption is suspect because the pit walls and the HLF have very different surface properties and elevations. These issues suggest the steady-state pit lake surface water elevation is underestimated. Moreover, based on neglect of the effect of the head of water on the pit floor, the seepage rate would be underestimated. The seepage rate to groundwater from the Erato pit lake is underestimated.

Solute transport simulations based on the estimated pit seepage fluxes underestimate potential impacts to groundwater and surface water (independent of uncertainties introduced by questionable source concentrations, other assumptions, and approach). Predictions of impacts require an integrated approach that includes loading of constituents to groundwater and surface water from all potential sources. The impacts assessment presented by Golder (2014d) only considers the loading from the mine pits and thus the overall impact on the groundwater cannot be adequately assessed.

Geochemical modeling of pit water runoff was performed to determine the quality of water reporting to sumps in the pits and ultimately to the PTS (GRE, 2014e) during operations. This pit water quality is also relevant to the lake that will develop in the Erato pit (and seep to groundwater) during operations (although the emphasis of the impacts analysis is on the post-closure period). The Erato pit will be partially backfilled with non-acid generating rock near the end of mining. The results of geochemical modeling the water quality of the backfilled Erato pit are summarized in Golder (2014e). This water quality is used in the post-closure impacts

---

[12] GRE, 2014. AMULSAR SITE 28 HEAP LEACH FACILITY WATER BALANCE CALCULATIONS.

analysis that includes seepage to groundwater from the backfilled Erato pit. Geochemical modeling of the water quality of the Tigranes-Artavasdes pit backfill seepage and Arshak pit seepage is summarized in GRE (2014f). These water quality results are also used in the post-closure impacts analysis.

2.1.3.3.1 Pit Water Runoff

Inappropriate results of the runoff water quality modeling (GRE, 2014e) can be illuminated with some examples of the multitude of issues identified with this modeling as noted below:

i. The chemistries of the waters contacting LV in the backfill (Tigranes-Artavasdes) and the pit walls are represented by ARD-74C HC test solutions (weeks 5 and 10, respectively), which were selected as purportedly conservative solutions. The solutions from this sample with 2.1% pyritic sulfur are not necessarily conservative, with many LV samples having more than 4% pyritic sulfur, ranging up to 9.5%. A better choice for conservatism would be the HC test solution from ARD-76C with 4.2% pyritic sulfur.

ii. The pH levels (3.7 for backfill and 3.5 for LV) at weeks 5 and 10 are high and chemical concentrations of the selected, less conservative ARD-74C solutions are very low, relative to solutions from weeks 14 to 20, when pH dropped to about 2.7. Sulfate, for example, increased from approximately 100 mg/L in weeks 5 and 10 to over 1,000 mg/L in later weeks. Iron increased from less than 10 mg/L to more than 150 mg/L. For the operations period, the rapid rate of mining is acknowledged in the choice of early HC test results.

iii. Three of the 4 initial solutions for simulated mixing of runoff waters (LV, backfill, VC, and colluvium) have significant charge imbalances (e.g., requiring nearly 7 mg/L chloride addition to VC), indicating poor and/or incomplete analyses. SiO_2 is missing for two solutions[13], and nitrogen species are missing for all solutions. Sodium (3.6 mg/L) was added to the backfill solution for charge balance. Changing concentrations significantly to charge balance solutions affects activity coefficients and saturation indices.

iv. The individual solutions were appropriately equilibrated with atmospheric oxygen and carbon dioxide, but many minerals, including multiple iron-bearing phases with saturation indices > 0 (Appendix C), were permitted to precipitate in each solution **before** mixing (i.e., as the water runs into the pit sumps). The iron phases include magnetite, hematite, and goethite, which have slow growth kinetics at surface temperatures (Zhu and Anderson, 2002). Cupric and cuprous ferrite (oxides) are also kinetically inhibited. These phases should not be specified to precipitate before or after mixing.

v. The mixed pit runoff water has extremely low iron concentrations (ferric iron 10^{-8} to 10^{-9} mg/L; ferrous iron 10^{-12} to 10^{-13} mg/L)[14] due to the strong mineralogic controls. For

---

[13] c.f., SiO2 for one LV SPLP is 8.3 mg/L, "Si" for Site 27 waste leachate is 11.3 mg/L, and Site 13 mine portal leachate is 12.1 mg/L (ESIA Appendix 4.6.2 Tables/Appendices D-1 and F-1).

[14] These concentrations are unrealistic and are less than iron concentrations in the Amulsar surface water, groundwater and rain water (Golder, 2019).

comparison, iron in Site 27 waste leachate with a pH of 3.3 is 3.2 mg/L (ESIA Appendix 4.6.2 Table/Appendix F-1). Silica (SiO_2) was not simulated.

2.1.3.3.2 Tigranes-Artavasdes Seepage and Arshak Pit Seepage

The water quality of seepage through the Tigranes-Artavasdes and Arshak pits (GRE, 2014f) were each modeled differently. The closure plan includes a 0.5-meter cover to minimize infiltration and oxygen penetration into the backfill of the Tigranes-Artavasdes pit. The modeling is based on the assumption that seepage water will only be impacted by the LV rock of the backfill. Assumptions include a limited zone of oxygen penetration in the backfill for ARD generation and equilibration of the seepage in the underlying anoxic zone of the backfill. In the Arshak pit, runoff water will collect at the bottom of the pit, where it is in contact with LV waste rock prior to seepage to groundwater. ARD generation on the pit walls and at the pit bottom are inputs to modeling anoxic conditions of the seepage below the pit bottom. Details of the modeling are not provided. However, some obvious deficiencies and inconsistencies are addressed below.

The compositions of HC test solutions were used to define initial solutions for runoff and seepage water. The loading rates were determined (GRE, 2014f) by averaging the weekly concentrations of all constituents, and then averaging each constituent's weekly averages. Concentrations are not loading rates. Loading rates are mass/unit mass per unit time. The loading rates were then multiplied by the total weight of rock and divided by the total seepage volume in order to simulate the initial seepage water quality. There is no discussion of the mass of rock contacted by seepage through the backfill, or assumptions about mass in contact with runoff on the pit walls (e.g., thickness), or the mass of backfill in contact with the runoff water at the bottom of the pit. Treatment of non-detectable concentrations was inconsistent. Sulfate was assigned ½ the detection limit and the other constituents were assigned zero. The text states that a buffer concentration was applied to alkalinity around detected values of 1 mg/L. This statement is not clear, and it appears that the stated concentration was arbitrarily assigned to solutions.

The description of oxygen diffusion modeling (GRE, 2014f) is cryptic and insufficient to evaluate. The oxygen consumption rates are reportedly taken from the geochemical modeling and are representative of the oxygen consumed by ARD reactions in the LV material. Based on that analysis, GRE derived an oxygen half-life of 700 days. The results of the oxygen consumption and oxygen diffusion modeling reportedly (GRE, 2014f) showed that oxygen penetration is limited to the uppermost 0.5 meter of the mine waste. However, GRE (2014f Figure 10) shows oxygen concentrations decreasing downward through 0.5 m of topsoil overlying backfill and arrows in the backfill point upward. Additionally, GRE (2014f) states that similar results were obtained for the Arshak pit bottom. Topsoil and fractured rock on the pit bottom have entirely different material properties. GRE (2014f) then states that the total depth of oxygen penetration is assumed to be 1.5 meters, consistent with results of analysis for the BRSF. This explanation is incomprehensible. The BRSF configuration is the same as the pit backfill, with soil overlying waste rock.

The procedures and resulting problems with the initial solutions are similar to the above description for the runoff modeling of the pits, e.g., use of ARD-74C HC week 10 test solution for the Arshak seepage and charge balancing with fluoride and sodium. After charge balancing each of the weekly HC solutions for the backfill, the text states the solutions were passed through the 1.5-meter-thick oxygenated zone of the waste rock (in contrast to the 0.5 m

Amulsar Gold Mine - Independent 3rd Party Assessment
Impacts on Water Resources, Geology, Biodiversity and Air Quality

July 22, 2019
55